Electronic supplementary information

Silver(I) complexes bearing heterocyclic thioamide ligands with NH_2 and CF_3 substituents: effect of ligand group substitution on antibacterial and anticancer properties

Despoina Varna,[a] Elena Geromichalou,[b] Antonios G. Hatzidimitriou,[a] Rigini Papi,[c] George Psomas,[a] Panagiotis Dalezis,[b] Paraskevas Aslanidis,[a] Theodora Choli-Papadopoulou,[c] Dimitrios T. Trafalis,[b,*] Panagiotis A. Angaridis[a,*]

[a] *Laboratory of Inorganic Chemistry, Department of Chemistry, Aristotle University of Thessaloniki, 54124 Thessaloniki, Greece*

[b] *Laboratory of Pharmacology, Medical School, National and Kapodistrian University of Athens, 75 Mikras Asias Street, 11527 Athens, Greece*

[c] *Laboratory of Biochemistry, Department of Chemistry, Aristotle University of Thessaloniki, Thessaloniki 54124, Greece*

TABLE OF CONTENTS

S1 EXPERIMENTAL

S1.1 General procedures and chemicals

All manipulations were carried out under atmospheric conditions, unless otherwise mentioned. Solvents were purified according to established methods and allowed to stand over molecular sieves for 24 h. Silver nitrate ($AgNO_3$), silver chloride (AgCl), 5-amino-1,3,4-thiadiazole-2-thione (atdztH), 4-methyl-5-(trifluoromethyl)-4H-1,2,4-triazol-3-thiol (mtftH), thriphenylphosphine (PPh_3), 4,5-bis(diphenylphosphino)-9,9-dimethylxanthene (xantphos), bis[(2-diphenylphosphino)phenyl] ether (DPEphos) were purchased from commercial sources and used as received.

For the *in vitro* antibacterial studies, four well-established bacterial strains (*E. coli, B. subtilis, B. cereus* and S. *aureus*) were used to explore the antibacterial activity of the studied complexes.

For the *in vitro* cytotoxicity studies, four well-established human cancer cell lines (human cancer ovarian SKOV-3, small cell lung cancer DMS114, prostate adenocarcinoma PC-3, and pancreatic adenocarcinoma HuP-T3 and a human normal lung cell line MRC5 were adopted to explore the anticancer activity of the studied complexes.

For the *in vitro* antioxidant activity studies, H_2O_2, 2,2-diphenyl-1-picryl-hydrazyl-hydrate (DPPH), and ABTS potassium persulfate, butylated hydroxytoluene, (BHT), 6-hydroxy-2,5,7,8-tetramethylchromane-2-carboxylic acid (trolox), nordihydroguaiaretic acid (NDGA) were obtained from commercial sources and used without any further purification.

For the *in vitro* biomolecule interaction studies CT DNA, BSA (bovine serum albumin), HSA (human serum albumin), EB (ethidium bromide), NaCl, trisodium citrate and solvents, were of reagent grade and were used as purchased from commercial sources without any further purification.

S1.2 Syntheses

S1.2.1 [AgCl(atdztH)(xantphos)] (1)

To a suspension of AgCl (0.043 g, 0.3 mmol) in 20 mL of CH_2Cl_2, the amount of 0.174 g (0.3 mmol) of xantphos was added and the mixture was stirred at 50°C for 20 min in dark. To the resulting suspension, atdztH (0.040 g, 0.3mmol) was added and the mixture was further stirred at 50°C for 2 h. After filtration to remove a small amount of grey solid, the filtrate was layered with hexane. In a period of 5 days, colorless crystals of **1** were formed which were collected. Yield (based on Ag): 0.122 g (48%). Anal. Calcd. for $[C_{42.25}H_{37.5}AgCl_{3.5}N_3OP_2S_2]$: % C, 48.95; H, 3.87; N, 3.94. Found: % C, 49.34; H, 4.07; N, 4.12. FTIR (KBr), $\tilde{\nu}/cm^{-1}$: 3429(br), 3121(w), 2908(w), 2751(w), 1617(m), 1560(s), 1491(m), 1479(m), 1434(s), 1402(vs), 1361(w), 1318(w), 1225(s), 1095(w), 1023(s), 953(w), 875(w), 743(s), 697(s), 509(s). ^{1}H NMR (500 MHz, $CDCl_3$), δ(ppm): 7.55-7.53 (d, 2H, xantphos), 7.36-7.33 (m, 8H, o-H, phenyl), 7.31-7.27 (d, 4H, p-H, phenyl), 7.23-7.20(t, 8H, m-H, phenyl),7.10-7.07 (t, 2H, xantphos), 6.66-6.58 (m, 2H, xantphos)1.67 (s, 6H, -CH_3). UV-Vis (CH_2Cl_2), λ/nm (log ε): 278 (4.29), 320 sh (3.27). Melting point: 209.1°C (decomp.).

S1.2.2 [Ag(μ-atdztH)(DPEphos)]$_2$(NO$_3$)$_2$ (2)

To a solution of $AgNO_3$ (0.051 g, 0.3 mmol) in a 30-mL mixture of CH_3CN/CH_3OH (1:1 v/v) DPEphos (0.162 g, 0.3 mmol) was added. The mixture was stirred at 70°C for 30 min until a colorless solution was formed and then 0.040 g (0.3 mmol) of atzdtH was added. After being stirred at 70°C for 2 h, the resulting mixture was allowed to cool at room temperature and then it was filtered. The filtrate was set aside to evaporate slowly at room temperature in dark. Large colorless crystals of **2** were obtained after 4 days which were collected. Yield (based on Ag): 0.289 g (62%). Anal. Calcd. for [$C_{79}H_{72}Ag_2Cl_2N_8O_{10}P_4S_4$]: % C, 47.92; H, 4.35; N, 5.26. Found: % C, 48.32; H, 4.12; N; 5.48. FTIR (KBr), $\tilde{\nu}/cm^{-1}$: 3441(br), 3055(w), 1619(m), 1561(w), 1480(w), 1460(m), 1435 (s), 1384(s), 1258(w), 1220(s), 1125(w), 1096(m), 1035(m), 988(m), 876(w), 799(w), 747(s), 694(s), 505(w). ^{1}H NMR (500 MHz, $CDCl_3$), δ(ppm): 7.72-7.60 (m, m-H, phenyl), 7.49-7.44 (m, p-H, phenyl), 7.41-7.30 (m, o-H, phenyl), 7.18-7.14 ppm (t, DPEphos), 7.10-7.07 ppm (t,DPEphos), 6.97-6.94 ppm (m,DPEphos), 6.83-6.81 ppm (m, DPEphos).UV-Vis ($CHCl_2$), λ/nm (log ε): 270 (4.04), 292 (3.98), 318 (3.80). Melting point: 178.3°C (decomp.).

S1.2.3 [Ag(atdzt)(PPh$_3$)$_3$]$_2$ (3)

$AgNO_3$ (0.051 g, 0.3 mmol) was dissolved in 10 mL of CH_3CN and PPh_3 (0.236 g, 0.9 mmol) was added. The mixture was stirred at room temperature for 20 min and then a solution of K^+atdzt^- obtained by addition of 1.6 mL of a 0.2 M methanolic solution of KOH into a solution of atdztH (0.040 g, 0.3 mmol) in 10 mL of CH_3OH, was added. After being stirred at room temperature for additional 2 h, the resulting mixture was was filtered and the filtrate was set aside to evaporate slowly in dark. Colorless crystals of **3** were obtained after 5 days, which were collected. Yield (based on Ag): 0.130 g (42%). Anal. Calcd. for [$C_{57}H_{48.50}AgN_{3.50}P_3S_2$]: % C, 65.36; H, 4.67; N, 4.68. Found: % C, 65.67; H, 4.95; N; 4.92. FTIR (KBr), $\tilde{\nu}/cm^{-1}$: 3441(br), 3055(w), 1619(m), 1561(w), 1480(w), 1460(m), 1435 (s), 1384(s), 1258(w), 1220(s), 1125(w), 1096(m), 1035(m), 988(m), 876(w), 799(w), 747(s), 694(s), 505(w). ^{1}H NMR (500 MHz, $CDCl_3$), δ(ppm): 7.69-7.65 (3H, p-H), 7.55-7.47 (6H, p-H), 7.38-7.33 (18H, o-H), 7.31-7.29 (18H, m-H). UV-Vis ($CHCl_2$), λ/nm (log ε): 260 (4.02), 340 (3.54). Melting point: 155.8°C (decomp.).

S1.2.4 [Ag(μ-atdzt)(DPEphos)]$_2$ (4)

$AgNO_3$ (0.051 g, 0.3 mmol) was suspended in 15 mL of CH_2Cl_2 and then DPEphos (0.162 g, 0.3 mmol) was added. in small portions and the contents were After stirring at room temperature for 30 min, a solution of K^+atdzt^- in CH_2Cl_2, obtained by addition of 1.6 mL of a 0.2 M methanolic solution of KOH into a solution of atdztH (0.040 g, 0.3 mmol) in 10 mL of CH_2Cl_2, was added. The reaction mixture was stirred for 2 h and then it was filtered. Colorless crystals of **4** were grown by layering the resulting filtrate with Et_2O over a period of 15 days, which were collected. Yield (based on Ag): 0.256 g (55%). Anal. Calcd. for [$C_{78}H_{66}Ag_2Cl_4N_6O_3P_4S_4$]: % C, 49.71; H, 3.75; N, 4.35. Found: % C, 50.01; H, 3.97; N; 4.57. FTIR (KBr), $\tilde{\nu}/cm^{-1}$: 3434(b), 3047(w), 1586(m), 1564(m), 1469(s), 1479(s), 1460(s), 1434(vs), 1378(s), 1296(w), 1258(w), 1223(vs), 1183(w), 1159(w), 1126(m), 1094(s), 1068(m), 1026(w), 996(m), 877(m), 798(m), 746(vs), 695(vs), 543(w), 531(w), 518(m), 506(m). ^{1}H NMR (500 MHz, $CDCl_3$), δ(ppm): 7.47-7.43 (m, 16H, o-H, phenyl), 7.35-7.33 (m, 8H, p-H, phenyl), 7.32-7.30 (m, 16H, m-H, phenyl), 7.17-7.14 (t, 2H, DPEphos), 6.95-6.92 (t, 2H, DPEphos), 6.79-

6.78 (d, 4H, DPEphos), 6.73-6.72 (d, 4H, DPEphos). UV-Vis (CH_2Cl_2), λ/nm (log ε): 280 (4.26). Melting point: 198.0°C (decomp.).

S1.2.5 [Ag(μ-mtfmt)(DPEphos)]$_2$ (5)

To a suspension of $AgNO_3$ (0.051 g 0.3 mmol) in 15 mL of CH_2Cl_2, DPEphos (0.162 g, 0.3 mmol) was added. The resulting mixture was stirred at room temperature for 30 min in dark and then a 10-mL methanolic solution of K^+mtfmt^- (0.060 g, 0.3 mmol) obtained from the deprotonation of the corresponding amount of mtfmtH with 1.6 mL of 0.19 M solution of KOH in CH_3OH, was added dropwise. After stirring at room temperature for 1 h, the reaction mixture was filtered. Large colorless crystals of **5** were obtained by layering the resulting filtrate with Et_2O over a period of 5 days. Yield (based on Ag): 0.318 g (65%). Anal. Calcd. for [$C_{80}H_{62}Ag_2F_6N_6O_2P_4S_2$]: % C, 57.98; H, 3.77; N, 5.07. Found: % C, 57.62; H, 3.43; N; 4.89. FTIR (KBr), $\tilde{\nu}/cm^{-1}$: 3044(br), 2364(w), 1580(m), 1565(m), 1513(s), 1479(s), 1460(s), 1434(vs), 1344(vs), 1270(m), 1222(s), 1191(vs), 1116(vs), 1082(s), 1019(w), 996(m), 959(w), 877(w), 746(vs), 695(vs), 531(w). ^{1}H NMR (500 MHz, $CDCl_3$), δ(ppm): 7.44-7.41 (m,8H, m-H, phenyl), 7.35-7.32 (m, 4H, p-H, phenyl), 7.30-7.23 (m, 8H, o-H, phenyl), 7.15-7.12 ppm (t, 2H, DPEphos), 6.93-6.90 ppm (t, 2H, DPEphos), 6.76-6.75 ppm (m, 2H, DPEphos), 6.70-6.68 ppm (m, 2H, DPEphos), 3.51(s, 3H, -CH_3). UV-Vis (CH_2Cl_2), λ/nm (logε): 267 (4.04), 290 (3.84). Melting point: 220.7°C (decomp.).

S1.3 Instrumentation

Elemental analyses were obtained on a PerkinElmer 240B elemental microanalyzer. Infra-red spectra were recorded on a Nicolet FT-IR 6700 spectrophotometer as KBr discs in the region of 4000-400 cm^{-1}. NMR. UV-Vis electronic absorption spectra were obtained on a Shimadzu 160A spectrophotometer as 1.0×10^{-6} M solutions in CH_2Cl_2. Emission/excitation fluorescence spectra were recorded both in solution and solid state on a Hitachi F-7000 fluorescence spectrometer. 1H NMR spectra were recorded in CDCl3 solutions on an Agilent 500 spectrometer. Chemical shifts were reported as δ values using the solvent as internal standard.

S1.4 Single crystal X-ray diffraction analysis

Single crystals of all complexes, suitable for X-ray crystallographic analysis, were mounted on thin glass fibers with the aid of an epoxy resin. X-ray diffraction data were collected on a Bruker Apex II CCD area-detector diffractometer, equipped with a Mo Ka (λ = 0.71070 Å) sealed tube source, at 295 K, using the φ and ω scans technique. The program Apex2 (Bruker AXS, 2006) was used in data collection, cell refinement, and data reduction.[1] Structures were solved and refined with full-matrix least-squares using the program Crystals.[2] Anisotropic displacement parameters were applied to all non-hydrogen atoms, while hydrogen atoms were generated geometrically and refined using a riding model. Details of crystal data and structure refinement parameters are shown in Table 1. Plots of the molecular structures of all complexes were obtained by using the program Mercury.[3]

S1.5 *In vitro* antibacterial activity

The *in vitro* antibacterial activity of **1**-**5** and their corresponding ligands towards *Escherichia coli* (*E. coli*) and *Bacillus subtilis* (*B. subtilis*), *Bacillus cereus* (*B. cereus*) and *Staphylococcus aureus* (*S. aureus*) bacterial strains, was evaluated using a method of using progressive double dilutions in MMS contained the concentrations of 100, 50, 25, 12.5, and 6.25 $\mu g \cdot mL^{-1}$ of the complexes in DMSO.[4] The growth of bacteria was estimated by measuring the turbidity of the culture, as previously reported [5]. Two cultivation media used for antibacterial activity tests were: (i) the Luria-Bertani broth [1% (w/v) tryptone, 0.5% (w/v) NaCl and 0.5% (w/v) yeast extract] and (ii) the minimal medium salts broth containing [1.5% (w/v) glucose, 0.5% (w/v) NH_4Cl, 0.5% (w/v) K_2HPO_4, 0.1% (w/v) NaCl, 0.01% (w/v) $MgSO_4 \cdot 7H_2O$]. The pH of the media was adjusted to 7.0.

S1.6 *In vitro* anticancer activity

S1.6.1 Cell culture

Complexes **1-5** were tested for their *in vitro* anticancer activity against four well-established human cancer cell lines (ovarian, lung, prostate, and pancreatic) and a human normal lung cell line. Ovarian cancer (SKOV-3) cells, small cell lung cancer (DMS114) cells, prostate adenocarcinoma (PC-3) cells, pancreatic adenocarcinoma (HuP-T3) cells, and normal lung (MRC5) cells, were tested for cytostatic (growth inhibition: IC_{50}, TGI) and cytotoxic/cytocidal (IC_{50}) activity against the tested complexes at concentrations of 0.5-100 μM. The cell lines were obtained from the American Type of Culture collection (ATCC), except HuP-T3 which was kindly donated from University of Crete, School of Medicine, Greece, and were grown in different culture medium according to the instructions. Cultures were maintained at 37 °C in 5 % CO_2 and 95 % air.

S 1.6.2 *In vitro* cytotoxicity assay

MTT assay was used to dermine the cell viability in presence of compound **1**-**5**. Cells were plated in 96-well plate at a density of 1×10^4 cells/mL per well and maintained for 72 h at 37 °C in a 5% CO_2 incubator and grown as monolayers. After 24 h, cells were treated with 0.5-150 μM of the tested complexes for 48 h. The viability of cultured cells was estimated by a (3-(4,5-imethylthiazol-2-yl)-2,5-diphenyltetrazolium bromide (MTT) metabolic assay as previously described [6,7,8].

In brief, MTT (Sigma, St Louis, Missouri, USA) was dissolved in PBS in a concentration of 5 mg/mL, filter sterilized, and stored at 4 °C. Then, 50 μL of stock solution was added to each culture and incubated for 3h at 37 °C. Formazan crystals were solubilized by DMSO (100 μL). Absorbance of the converted dye was measured at a wavelength of 540 nm on ELISA reader (VersaMax Microplate Reader Orleans, USA). The mean concentrations of each drug that generated 50% or total (100%) growth inhibition (GI_{50} and TGI, respectively) as well as the drug concentrations that produced cytotoxicity against 50 % of the cultured cells [half maximal inhibitory concentration (IC_{50})] were calculated using the linear regression method [7]. Using seven absorbance measurements [time 24 h (Ct24), control growth 72 h (Ct72), and test growth in the presence of drug at five concentration levels (Tt72x)], the percentage of growth was calculated at each level of the drug concentrations. The percentage growth inhibition was calculated according to National Cancer Institute (NCI) as: {[(Tt72x)–(Ct24)]/[(Ct72)–(Ct24)]}×100 for concentrations for which Tt72x>Ct24 and {(Tt72x)–(Ct24)] / (Ct24)}×100 for concentrations for which Tt72x<Ct24. The GI_{50} was calculated from {[(Tt72x)–(Ct24)] / [(Ct72)–

(Ct24)]}×100 = 50 while the TGI from {[(Tt72x)–(Ct24)] / [(Ct72)–(Ct24)]}×100 = 0, and IC_{50} from {[(Tt72x)–(Ct24)]/(Ct24)}×100 = 50. All experiments were carried out in triplicate. A significant difference was presumed to exist when $p \leq 0.05$ (two tailed paired *t* test).

S1.7 *In vitro* antioxidant activity

In vitro antioxidant activity studies for **1**-**5** and their ligands in their free form, were performed in order to determine their ability to scavenge hydroxyl, DPPH, and ABTS free radicals and was compared with the antioxidant capacity of reference compounds (NDGA, BHT, trolox and ascorbic acid). All measurements were carried out in triplicate and the standard deviation of absorbance was < 10% of the mean.

S1.7.1 Reduction of hydrogen peroxide

The antioxidant activity of the **1**-**5** and their corresponding ligands (atdztH, mtftH PPh_3, xantphos, DPEphos) in free form, against hydrogen peroxide was determined by monitoring the reduction of H_2O_2. The reaction mixture contained 20 μL of each of the tested complexes (0.1 mM) and 5 μL H_2O_2 solution (40 mM) in phosphate buffer (50 mM, pH 7.4). The absorbance was measured at 230 nm after 20 min. The antioxidant activity of the complexes was expressed as percent reduction of hydrogen peroxide (%H_2O_2) [9]. Ascorbic acid (or vitamin C) was used as an appropriate standard.

S1.7.2 Determination of the reducing activity of DPPH radical

To a methanolic solution of DPPH (0.1 mM) an equal volume solution of the complexes (0.1 mM) in methanol was added. Absolute methanol was also used as control solution. The absorbance at 517 nm was recorded at room temperature after 30 and 60 min, in order to examine the possible existence of a potential time-dependence of the DPPH radical scavenging activity [51]. The DPPH scavenging activity of the complexes was expressed as the percentage reduction of the absorbance values of the initial DPPH solution (RA %). NDGA and BHT were used as reference compounds.

S1.7.3 Assay of radical cation ABTS scavenging activity

Initially, a water solution of ABTS was prepared (2 mM). ABTS radical cation (ABTS+%) was produced by the reaction of ABTS stock solution with potassium persulfate (0.17 mM) and the mixture was stored in the dark at room temperature for 12–16 h before its use. The ABTS was oxidized incompletely because the stoichiometric reaction ratio of ABTS and potassium persulfate is 1:0.5. The absorbance became maximal and stable only after > 6 h of reaction although the oxidation of the ABTS started immediately. The radical was stable in this form for > 2 days when allowed to stand in the dark at room temperature. Afterwards, the ABTS+% solution was diluted in ethanol to an absorbance of 0.70 at 734 nm and 200 μL of diluted compounds or standards (0.1 mM) in DMSO were added. The absorbance was recorded out exactly 15 min after initial mixing [51]. The radical scavenging activity of the complexes was expressed as the percentage inhibition of the absorbance of the initial ABTS solution (ABTS %). Trolox was used as an appropriate standard.

S1.8 CT-DNA interaction

In vitro interaction of **1**-**3** with CT-DNA was evaluated with UV-vis absorption spectroscopy. The potential binding mode of the complexes and their corresponding binding constants (K_b) were also determined. Additional control experiments with 5% DMSO (v/v) did not lead to any changes in the spectra of CT DNA. The UV-vis spectra of CT-DNA solution (1.5×10^{-4} M) were recorded in the presence of each compound at diverse [compound]/[CT-DNA] mixing ratios (*r*). In parallel, the UV-vis spectra of the **1**-**3** were recorded for

a standard concentration (10-50 μM) in the presence of increasing amounts of CT-DNA at diverse [DNA]/[complex] ratios r′. The DNA-binding constant (K_b, in M^{-1}) was obtained by monitoring the changes in the absorbance at the corresponding λ_{max} with increasing concentrations of CT-DNA and it is given by the ratio of slope to the y intercept in plots [DNA]/(ε_A-ε_f) *versus* [DNA], according to the Wolfe- Shimer equation [1]:

$$\frac{[DNA]}{(\varepsilon_A - \varepsilon_f)} = \frac{[DNA]}{(\varepsilon_b - \varepsilon_f)} + \frac{1}{K_b(\varepsilon_b - \varepsilon_f)} \quad \text{(eq. S1)}$$

where [DNA] is the concentration of DNA in base pairs, $\varepsilon_A = A_{obsd}/[compound]$, ε_f = the extinction coefficient for the free compound and ε_b = the extinction coefficient for the compound in the fully bound form.

The viscosity of DNA ([DNA] = 0.1 mM) in buffer solution (150 mM NaCl and 15 mM trisodium citrate at pH 7.0) was measured in the presence of increasing amounts of complexes 1-6 (up to the r value = 0.35). All measurements were performed at room temperature. The obtained data are presented as $(\eta/\eta_0)^{1/3}$ versus r, where η is the viscosity of DNA in the presence of the compound, and η_0 is the viscosity of DNA alone in buffer solution. DNA-length (L/L_0), according to the equation $L/L_0 = (\eta/\eta_0)^{1/3}$. In general, the observed changes of the relative DNA-viscosity occurring in the presence of increasing amounts of the compound 1-3 which interact with CT-DNA, reveal subsequently the possible binding mode. In the particular case of intercalation, an increase in the separation distance of the DNA-base pairs can be induced in order to host the inserting compound resulting in an increase of the relative DNA-viscosity. On the other hand, when a compound binds to DNA-grooves via non-classic intercalation (i.e.electrostatic interaction or external groove-binding) the DNA-viscosity may show a slight decrease or remain unchanged, because of a bend of DNA double helix which leads to shortening of DNA length.[10]

Fluorescence emission spectroscopy was carried out to determine the ability of **1**-**3** to compete EB for the DNA-intercalating sites and displacing it from the EB-DNA conjugate [11]. The EB-DNA complex was prepared by adding 20 μM EB and 26 μM CT DNA in buffer solution (150 mM NaCl and 15 mM trisodium citrate at pH 7.0). The potential EB-displacing ability of the complexes was studied by a stepwise addition of a compound's solution into the EB-DNA solution. The resultant changes were monitored by recording the variation of fluorescence emission spectra with excitation wavelength at 540 nm. The complexes did not exhibit any appreciable fluorescence emission bands at room temperature in solution or in the presence of DNA or EB under the same experimental conditions (λ(exc) = 540 nm); therefore, the observed quenching may be attributed to the displacement of EB from its EB-DNA conjugate. The Stern-Volmer constant (KSV, in M^{-1}) is used to evaluate the quenching efficiency for each compound according to the Stern-Volmer equation (Eq. (2)) [12,13]

$$\frac{Io}{I} = 1 + k_q\tau_0[Q] = 1 + K_{SV}[Q] \quad \text{(Eq. S2)}$$

where I_o and I are the emission intensities of the EB-DNA solution in the absence and the presence of the quencher, respectively, [Q] is the concentration of the quencher , τ_o = the average lifetime of the emitting system without the quencher and k_q = the quenching constant. K_{SV} may be obtained from the Stern-Volmer plots by the slope of the diagram Io/I *versus* [Q]. Taking τ_o = 23 ns as the fluorescence lifetime of the EB-

DNA system [3], the quenching constants (k_q, in $M^{-1}s^{-1}$) of the complexes can be determined according to eq. S3.

$$K_{SV} = k_q\tau_o \text{ (Eq. S3)}$$

S1.9 Serum albumins binding

The serum albumin (SA) binding study was performed by tryptophan fluorescence quenching experiments using BSA (3 μM) or HSA (3 μM) in buffer (containing 1 mM trisodium citrate and 150 mM NaCl at pH 7.0). The quenching of the emission intensity of tryptophan residues of BSA at 340 nm or HSA at 350 nm was monitored using **1**-**3** as quenchers at increasing concentrations. The fluorescence emission spectra were recorded from 300 to 500 nm at excitation wavelength of 295 nm. The solution of complexes exhibited a very-low-intensity emission band at 330 nm, upon excitation at 295 nm. The fluorescence emission spectra of **1**-**3** were subtracted from the SA-emission spectra in order to proceed to calculating of the corresponding constants.

In the meanwhile, the influence of the inner-filter effect on the measurements was negligible as evaluated by the equation:

$$I_{corr}=I_{meas}\times 10^{\frac{\varepsilon_{\lambda(exc)}cd}{2}}\times 10^{\frac{\varepsilon_{\lambda(em)}cd}{2}} \text{ (eq. S4)}$$

where I_{corr} = corrected intensity, I_{meas} = the measured intensity, c = the concentration of the quencher, d = the cuvette (1 cm), $\varepsilon_{\lambda(exc)}$ and $\varepsilon_{\lambda(em)}$ = the ε of the quencher at the excitation and the emission wavelength, respectively, as calculated from the UV-Vis spectra of the complexes [S4].

The Stern-Volmer and Scatchard graphs are used in order to study the interaction of a quencher with serum albumins. According to Stern-Volmer quenching equation (eq. S2) [S2], where I_o = the initial tryptophan fluorescence intensity of SA, I = the tryptophan fluorescence intensity of SA after the addition of the quencher, k_q = the quenching constant, K_{SV} = the Stern-Volmer constant, τ_o = the average lifetime of SA without the quencher, [Q] = the concentration of the quencher. K_{SV} (M^{-1}) can be obtained by the slope of the diagram I_o/I versus [Q], and subsequently the quenching constant (k_q, $M^{-1}s^{-1}$) is calculated from equation (eq. S3) with τo = 10^{-8} s as fluorescence lifetime of tryptophan in SA.

From the Scatchard equation [S5]:

$$\frac{\Delta I/_{Io}}{[Q]} = nK - k\frac{\Delta I}{Io} \text{ (eq. S5)}$$

where, n is the number of binding sites per albumin and K is the SA-binding constant. K (in M^{-1}) is calculated from the slope in plots $\frac{\Delta I/_{Io}}{[Q]}$ *versus* $\frac{\Delta I}{Io}$ and n is given by the ratio of y intercept to the slope [S5].

S1.10 *In silico* molecular docking calculations

The *in silico* predictive tools that have been employed to study the interaction of the complexes with the selected macromolecules, are Schrödinger, Mercury, Spartan ’14, and PyMOL molecular modeling software. The synthesized complexes were generated from their X-ray crystal structures as CIF files. Mercury software (http://www.ccdc.cam.ac.uk/) was then used to convert the CIF files to PDB format files. The best, most stable (lowest energy) conformation of each molecular model of the complexes was detected by geometrical optimization in the gas phase, as implemented in the Spartan ’14 Molecular Modeling program suite [14]. The structure was initially optimized (*via* energy minimization) by conformational search using the Monte Carlo method with the MMFF94 molecular mechanics model, included in the Spartan’14 program suite. Geometry optimization (leading to the most stable conformer with the lowest energy) was accomplished *via* quantum-chemical calculations by utilizing the *ab initio* Hartree-Fock method with a 6-31G* basis set. Molecular docking was carried out on the crystal structure of the following target macromolecules: E. coli and S. aureus DNA-gyrase (PDB entry codes 1KZN and 5CDM, respectively), and fibroblast growth factor receptor (FGFR1) (PDB entry code 4V04), to investigate the effect of the complexes on these targets. X-ray crystal structures of *E. coli* DNA gyrase in complex with bound co-crystallized drug chlorobiocin (CBN) [15], *S. aureus* DNA gyrase in complex with bound co-crystallized drugs moxifloxacin (MFX) and QPT-1 [16], and FGFR1 in complex with its inhibitor drug ponatinib [17]were obtained from the Brookhaven Protein Data Bank (operated by the Research Collaboratory for Structural Bioinformatics, RCSB) [18, 19, 20]. The crystal structures of *E. coli* and *S. aureus* DNA gyrase enzymes have been refined at 2.3 Å and 2.5 Å resolution, respectively, while the crystal structure of FGFR1 bound with ponatinib at 2.12 Å resolution. For the docking calculations on the kinase domain of FGFR1 it was used only the A chain of the protein since chain B is replicate, with ponatinib (0LI) FGFR1 inhibitor bound at the same ligand binding site among the chains. For this reason, from the corresponding PDB files, the data for chain B and the data of the drugs referring to this chain were deleted. In our studies, molecular docking calculations were performed with Schrödinger modeling suite having the ability for accurate calculations. The Schrödinger software suite contains a broad array of computational chemistry tools. In the procedure for molecular docking with the employment of Schrödinger suite all complexes were sketched and converted into three-dimensional MOL2 files using Schrödinger Release 2015-2 Maestro Version 10.5 and minimized using LigPrep 3.4 [21] (which can generate a number of structures from each input structure with various ionization states, tautomers, stereochemical characteristics, and ring conformations to eliminate molecules on the basis of various criteria such as molecular weight or specified numbers and types of functional groups with correct chiralities for each successfully processed input structure), and the OPLS3 (**O**ptimized **P**otential for **L**iquid **S**imulations) [22] force field for the optimization, producing the low-energy isomers of the ligands [23]. Energy minimized 3D molecular structures were generated with the employment of LigPrep run from Maestro utility of the Schrödinger suite. The ligand preparation included 2D–3D conversions, generating variations, correction, verification and optimization of the structures. A preparation of receptor and ligand structures was integrated before the actual docking procedure [24].The crystal structures of the proteins were prepared using the Protein Preparation Wizard [24] in Schrödinger Suite 2015-2 (Schrödinger, LLC, New York, NY) [25, 26].Protein was prepared by adding the

hydrogen atoms, optimizing hydrogen bonds, removing atomic clashes, adding formal charges to the hetero groups and then optimizing at neutral pH. Missing loops and side chains were prepared using Prime version 3.2 [27]. Finally, the structure was minimized using OPLS3 force field. Active site of studied proteins was obtained using SiteMap tool [28, 29], which provides a fast and effective means of identifying potential binding pockets of proteins. SiteMap identifies the character of binding sites using novel search and assesses each site by calculating various properties like size, volume, amino acid exposure, enclosure, contact, hydrophobicity, hydrophilicity and donor/acceptor ratio. Receptor grid was generated around the active site for effective binding using Receptor grid generation in the Glide (version 5.9) application of Maestro. Once the receptor grid is generated, the ligands are docked to the proteins using Glide docking tool of Schrödinger (**G**rid based **LI**gand **D**ocking with **E**nergetics) [30]. Complexes were docked in the binding site of the proteins using Induced-Fit Docking (IFD) protocol 2015-2 [31]. The ligand interactions are shown in Ligand interaction tool of Maestro (Schrödinger). Waters were deleted with Maestro, the graphical user interface (GUI) of Schrödinger software, prior to docking. Molecular docking studies were carried out for the best fitted complexes to the model, while the final selection criteria were complexes docking scores and the presence of crucial interactions for binding to the studied proteins [32].The resulting poses were examined manually and the most promising ones were redocked with IFD calculations. Poses that pass the initial screens enter the final stage of the algorithm, which involves evaluation and minimization of a grid approximation to the OPLS-AA nonbonded ligand-receptor interaction energy. Final scoring is then carried out on the energy-minimized poses. By default, Schrödinger's proprietary GlideScore [30] multi-ligand scoring function is used to score the poses. All complexes showed good docking scores reflecting drug-binding affinities with the studied proteins. The PyMol Molecular Graphics System (Schrödinger, LLC. version 1.8.2.0, www.pymol.org), was used to visualize the molecules and analyze the results of the docking and to construct the molecular models [33].

S2 RESULTS

S2.1 Single crystal X-ray diffraction analysis

Table S1. Crystal data, data collection, and refinement parameters for **1**, **2**, **4**, and **5**.

	1·1.25 CH_2Cl_2	**2**·CH_2Cl_2·2CH_3OH
Chemical formula	$C_{169}H_{150}Ag_4Cl_{14}N_{12}O_4P_8S_8$	$C_{79}H_{72}Ag_2Cl_2N_8O_{10}P_4S_4$
Formula weight	3845.25	1832.29
Crystal system	Monoclinic	Triclinic
Space group	$P2_1/c$	P-1
Temperature (K)	295	295
Unit cell parameters		
a (Å)	11.9134 (19)	13.3274(15)
b (Å)	17.617 (3)	13.6558 (16)
c (Å)	23.058 (4)	15.1027 (16)
α (°)	90	66.660(5)
β (°)	96.416(5)	63.967(5)
γ (°)	90	77.579(6)
Volume (Å^3)	4809.3 (13)	2264.8 (5)
Z	1	1
Radiation type, *λ* (Å)	Mo Kα	Mo Kα
Absorption coefficient (mm^{-1})	0.80	0.71
Crystal size (mm)	0.23 × 0.17 × 0.16	0.25 × 0.23 × 0.17
Absorption correction	Numerical Analytical Absorption (De Meulenaer & Tompa, 1965)	Numerical Analytical Absorption (De Meulenaer & Tompa, 1965)
T_{min}, T_{max}	0.87, 0.88	0.85, 0.89
Number of measured, independent and observed [$I > 2.0\sigma(I)$] reflections	52787, 9153, 5798	46525, 8697, 5682
R_{int}	0.026	0.057
$(\sin\theta/\lambda)_{max}$ (Å^{-1})	0.611	0.614
$R[F^2>2\sigma(F^2)]$, $wR(F^2)$, S	0.050, 0.123, 1.00	0.048, 0.100, 1.00
No. of reflections	5798	5682
No. of parameters	493	502
$\Delta\rho_{max}$, $\Delta\rho_{min}$ (e Å^{-3})	1.54, −2.13	0.68, −0.44

(continued)

(continued)

	4·CH_2Cl_2·0.5H_2O	5
Chemical formula	$C_{78}H_{66}Ag_2Cl_4N_6O_3P_4S_4$	$C_{80}H_{62}Ag_2F_6N_6O_2P_4S_2$
Formula weight	1745.13	1657.16
Crystal system	Triclinic	Triclinic
Space group	P-1	P-1
Temperature (K)	295	295
Unit cell parameters		
a (Å)	13.2769 (9)	12.2334 (4)
b (Å)	13.8823 (11)	13.1115 (5)
c (Å)	14.9385 (18)	14.1839 (6)
α (°)	108.182 (5)	116.6650 (18)
β (°)	99.351 (5)	96.1758 (19)
γ (°)	118.341 (3)	110.5315 (18)
Volume (Å^3)	2137.6 (4)	1806.01 (13)
Z	1	1
Radiation type, *λ* (Å)	Mo Kα	Mo Kα
Absorption coefficient (mm^{-1})	0.80	0.76
Crystal size (mm)	0.26×0.22×0.19	0.24×0.18×0.17
Absorption correction	Numerical Analytical Absorption (De Meulenaer & Tompa,	Numerical Analytical Absorption (De Meulenaer & Tompa,
T_{min}, T_{max}	0.84, 0.86	0.87, 0.88
Number of measured, independent and observed [I> 2.0σ(I)] reflections	42025, 8270, 6132	37478, 6913, 4732
R_{int}	0.023	0.059
$(\sin \theta/\lambda)_{max}$ (Å^{-1})	0.616	0.613
$R[F^2>2\sigma(F^2)]$, $wR(F^2)$, S	0.040, 0.079, 1.00	0.044, 0.061, 1.00
No. of reflections	6132	4732
No. of parameters	457	460
$\Delta\rho_{max}$, $\Delta\rho_{min}$ (e Å^{-3})	0.62, −0.74	1.61, −0.87

Table S2. Selected bond distances (Å) and bond angles (º) for **1**.

Bond distances (Å)			
Ag1–P1	2.517(2)	Ag1–S1	2.647(1)
Ag1–P2	2.471(1)	Ag1–Cl1	2.612(2)
Bond angles (°)			
P1–Ag1–P2	111.32(4)	P1-Ag1-Cl1	116.47(5)
P1–Ag1–S1	100.72(4)	P2-Ag1-Cl1	105.18(5)
P2–Ag1–S1	123.44(5)	S1–Ag–Cl1	99.97(5)
Ag1–S1–C1	112.4(3)		

Table S3. Selected bond distances (Å) and bond angles (º) for **2**, **4** and **5**.

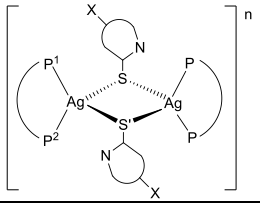

	X = NH_2, n = +1 **2**	X = NH_2, n = 0 **4**	X = CF_3, n = 0 **5**
Bond distances (Å)			
Ag1–P1	2.536(1)	2.483(1)	2.515(1)
Ag1–P2	2.465(1)	2.505(1)	2.530(1)
Ag1–S1	2.612(2)	2.580(1)	2.587(1)
Ag1–S1′	2.683(1)	2.620(1)	2.679(2)
S1–C1	1.710(5)	1.647(4)	1.721(6)
Ag···Ag	3.513(1)	3.514(1)	3.341(1)
Bond angles (°)			
P1–Ag1–P2	108.64(5)	109.39(4)	113.07(4)
P1–Ag1–S1	112.98(4)	112.54(4)	103.54(4)
P1–Ag1–S1′	87.97(4)	121.10(4)	122.21(4)
P2–Ag1–S1	114.69(5)	117.16(4)	120.89(4)
P2–Ag1–S1′	132.83(5)	101.10(4)	96.57(4)
S1–Ag1–S1′	96.90(5)	95.00(3)	101.25(4)
Ag1–S1–C1	98.65(18)	113.6(2)	108.48(15)
Ag1–S1–Ag1′	83.10(5)	85.00(4)	78.75(4)
C1–S1′–Ag1	120.17(18)	107.52(16)	115.65(14)

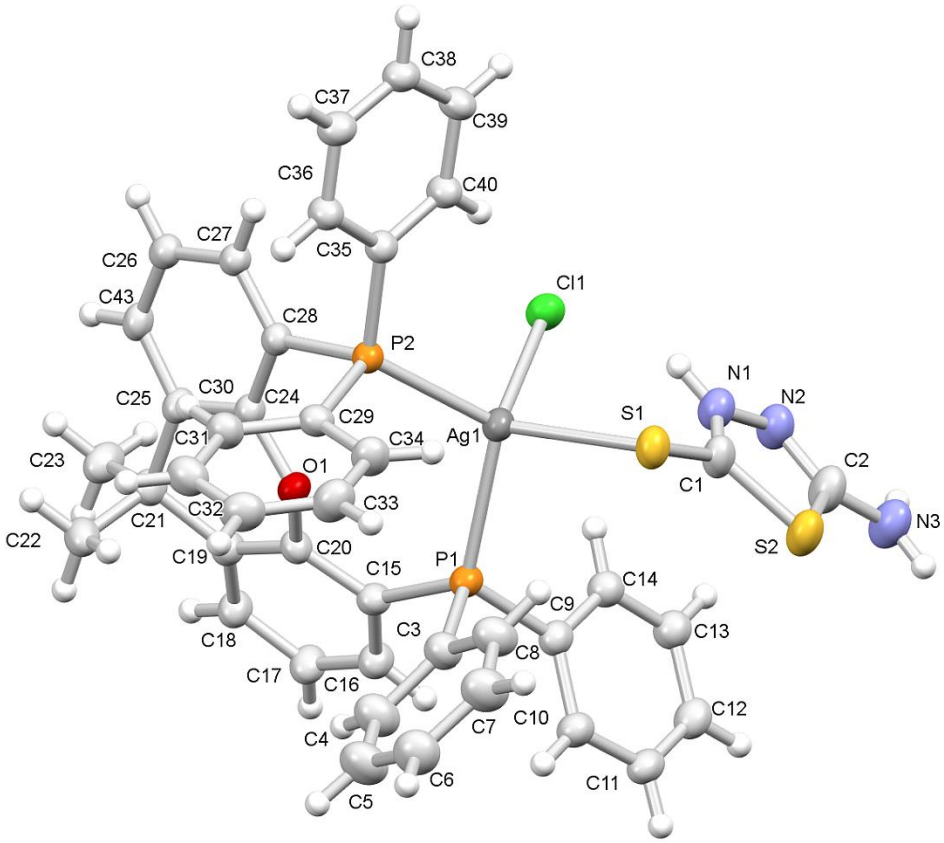

Figure S1. View of the crystal structure of [AgCl(atdztH)(xantphos)Cl] (**1**). Atoms are presented as thermal ellipsoids at the 35% probability level, while hydrogen atoms are shown as spheres of arbitrary radius.

Table S4. Selected bond lengths (Å) and angles (°) for **1**.

Bond distances (Å)			
Ag1–P1	2.517(2)	Ag1–Cl1	2.612(2)
Ag1–P2	2.471(1)	S1–C1	1.679(6)
Ag1–S1	2.647(1)		
Bond angles (°)			
P1–Ag1–P2	111.32(4)	P1-Ag1-Cl1	116.47(5)
P1–Ag1–S1	100.72(4)	P2-Ag1-Cl1	105.18(5)
P2–Ag1–S1	123.44(5)	Cl1–Ag–S1	99.97(5)
Ag1–S1–C1	112.4(3)		

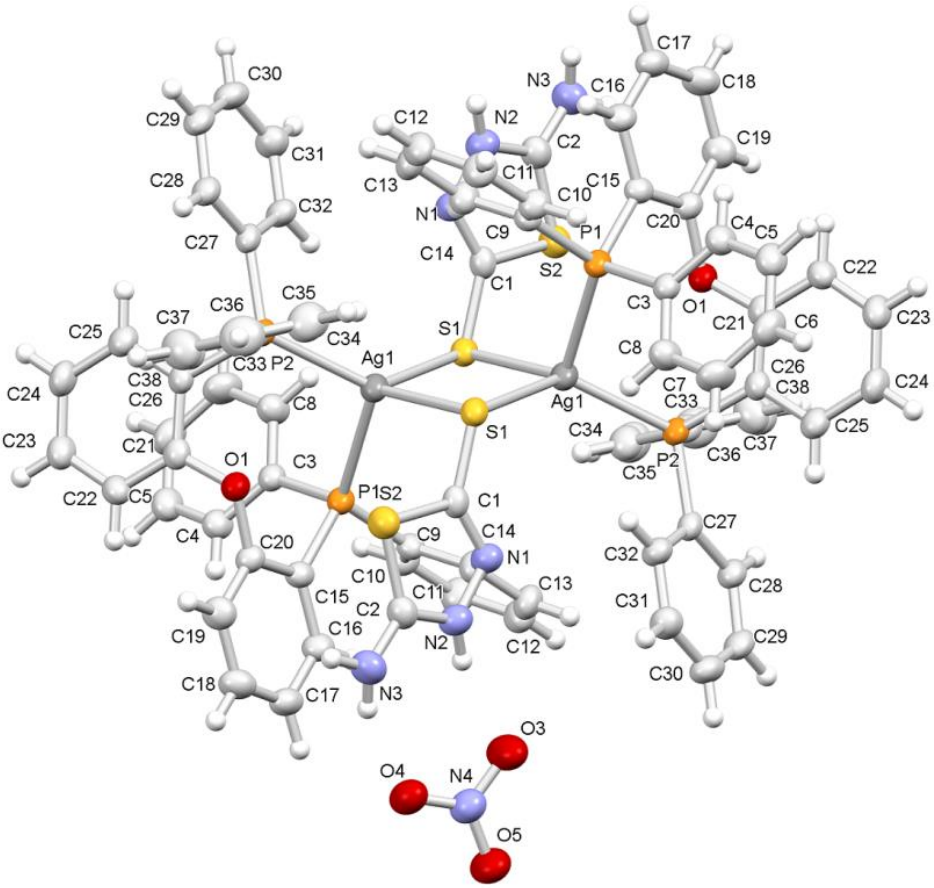

Figure S2. View of the crystal structure of $[Ag(\mu\text{-atdztH})(DPEphos)]_2(NO_3)_2$ (**2**) (only one of the NO_3^- counterions is shown). Atoms are presented as thermal ellipsoids at the 35% probability level, while hydrogen atoms are shown as spheres of arbitrary radius.

Table S5. Selected bond lengths (Å) and angles (°) for **2**.

Bond distances (Å)			
Ag1–P1	2.536(1)	Ag1–S1′	2.683(1)
Ag1–P2	2.465(1)	S1–C1	1.710(5)
Ag1–S1	2.612(2)		
Bond angles (°)			
P1–Ag1–P2	108.64(5)	Ag1–S1–C1	98.65(18)
P1–Ag1–S1	112.98(4)	S1–Ag1–S1′	96.90(4)
P1–Ag1–S1	87.97(4)	Ag1–S1–Ag1′	83.10(4)
P2–Ag1–S1′	114.69(5)	C1–S1′–Ag1	120.17(18)
P2–Ag1–S1	132.83(5)		

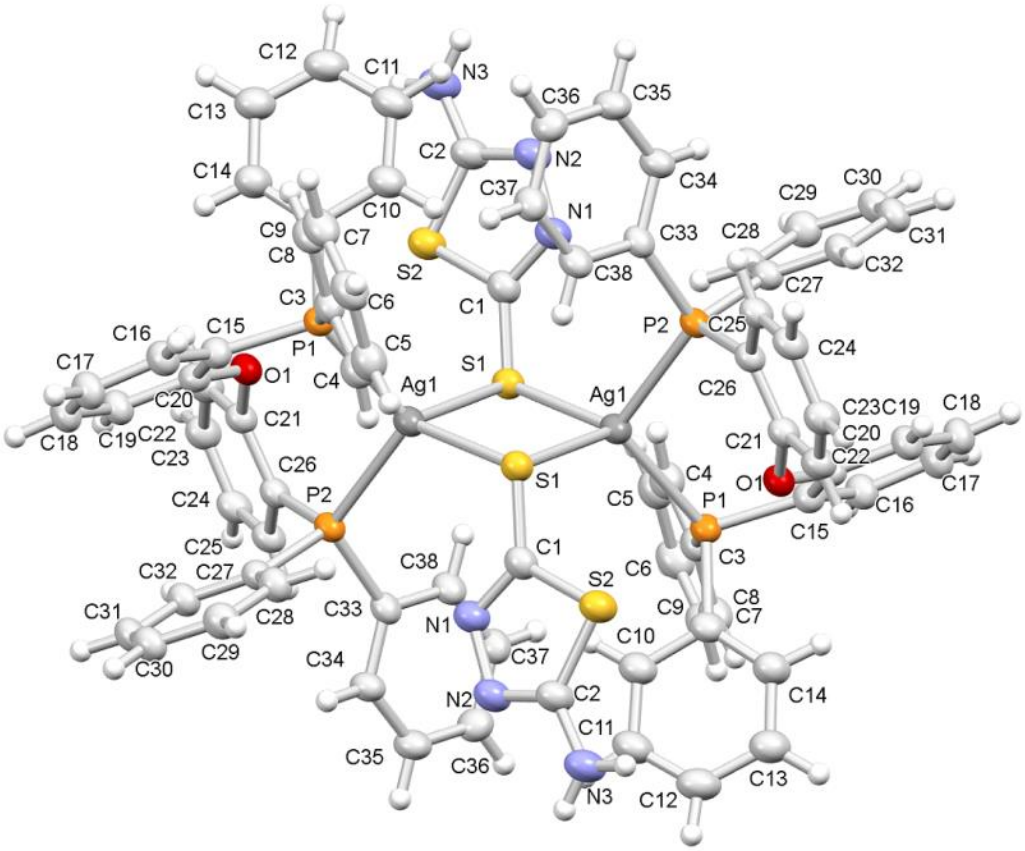

Figure S3. View of the crystal structure of [Ag(μ-atdztH)(DPEphos)]$_2$ (**4**). Atoms are presented as thermal ellipsoids at the 35% probability level, while hydrogen atoms are shown as spheres of arbitrary radius.

Table S6. Selected bond lengths (Å) and angles (°) for **4**.

Bond distances (Å)			
Ag1–P1	2.483(1)	Ag1–S1′	2.620(1)
Ag1–P2	2.505(1)	S1–C1	1.647(4)
Ag1–S1	2.580(1)		
Bond angles (°)			
P1–Ag1–P2	109.39(4)	S1–Ag1–S1′	95.00(3)
P1–Ag1–S1	112.54(4)	Ag1–S1–C1	113.6(2)
P1–Ag1–S1′	121.10(4)	Ag1–S1–Ag1′	85.00(4)
P2–Ag1–S1	117.16(4)	C1–S1′–Ag1	107.52(16)
P2–Ag1–S1′	101.10(4)		

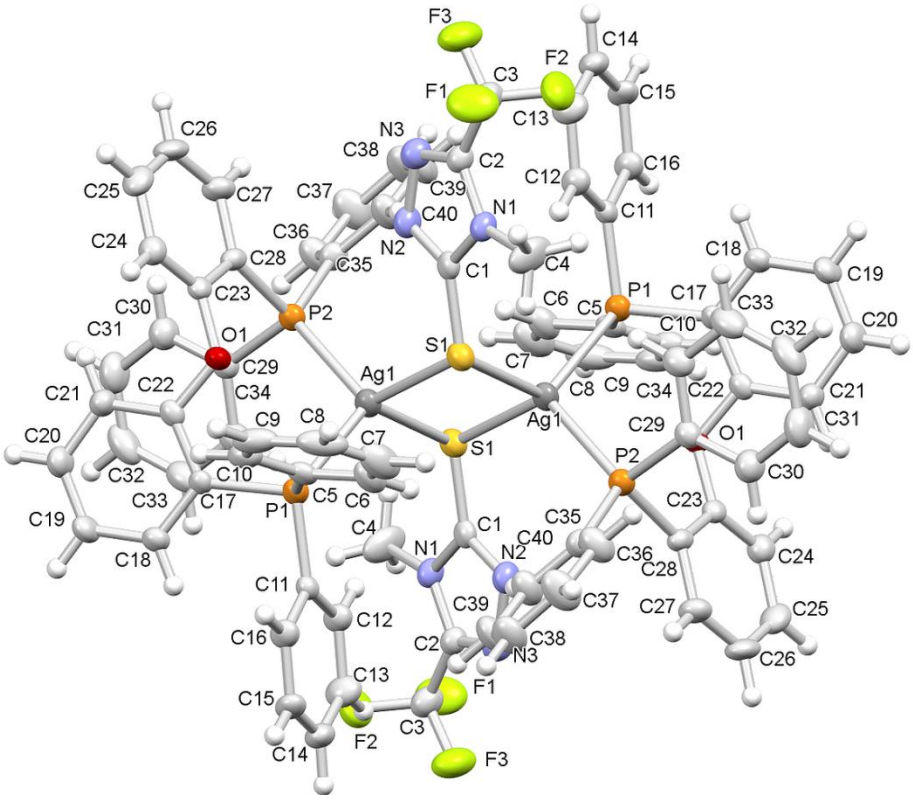

Figure S4. View of the crystal structure of [Ag(μ-mtft)(DPEphos)]$_2$ (**5**). Atoms are presented as thermal ellipsoids at the 35% probability level, while hydrogen atoms are shown as spheres of arbitrary radius.

Table S7. Selected bond lengths (Å) and angles (°) for **5**.

Bond distances (Å)			
Ag1–P1	2.515(1)	Ag1–S1′	2.679(2)
Ag1–P2	2.530(1)	S1–C1	1.721(6)
Ag1–S1	2.587(1)		
Bond angles (°)			
P1–Ag1–P2	113.07(4)	S1–Ag1–S1′	101.25(4)
P1–Ag1–S1	103.54(4)	Ag1–S1–C1	108.48(15)
P1–Ag1–S1′	122.21(4)	Ag1–S1–Ag1′	78.75(4)
P2–Ag1–S1	120.89(4)	C1–S1′–Ag1	115.65(14)
P2–Ag1–S1′	96.57(4)		

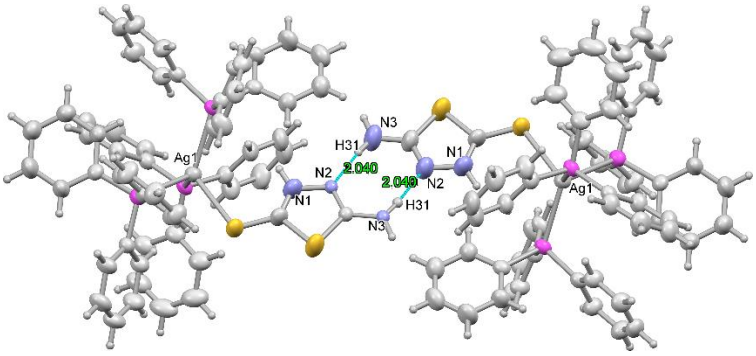

(a)

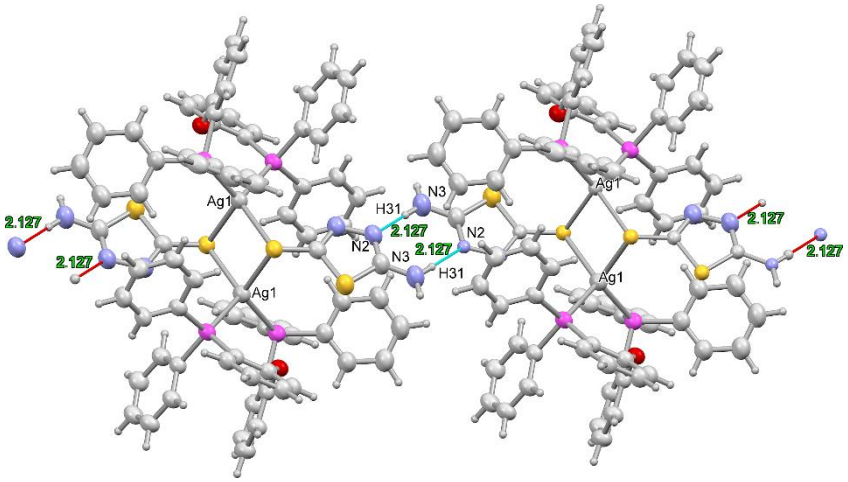

(b)

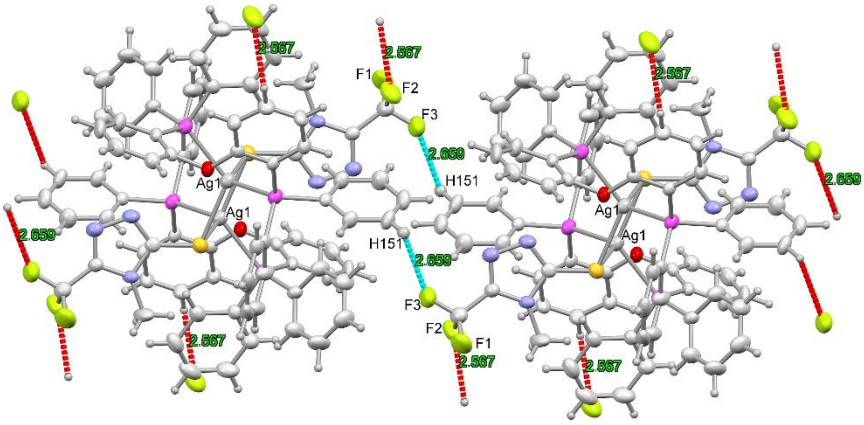

(c)

Figure S5. Views of the solid-state structures of (a) **3**, (b) **5**, and (c) **6**, showing the intermolecular H-bonding and short atom contacts that are present in each case, which result in the formation of extended molecular architectures.

S2.2 Stability in solution

S2.2.1 Stability study followed by ^{1}HMR spectroscopy

The ^{1}H NMR spectrum of the dicationic complex [Ag(μ-atdztH)(DPEphos)]$_2$(NO_3)$_2$ (**2**) exhibits a set of multiplets in the 7.72-6.80 ppm region attributed to the H's of the phenyl groups of DPEphos, slightly shifted to lower field than the corresponding signals that appear in the spectrum of the ligand in free form. However, these signals are not well resolved giving an indication of a potential dynamic behavior of the molecule in its solution. In case of the neutral complex [Ag(μ-atdzt)(DPEphos)]$_2$ (**4**), a set of unresolved multiplets appearing between 7.43 ppm and 6.72 ppm are ascribed to H's of phenyl groups of the diphosphine ligand. Interestingly, in the 1H NMR spectrum of [Ag(μ-mtft)(DPEphos)]$_2$ (**5**), signals of the H's of the phenyl groups of DPEphos appear well-resolved for their ortho, meta and para H signals in the 7.44-7.23 ppm region. In addition, H's of the DPEphos backbone give resolved signals at slightly higher field in the 7.15-6.68 ppm region, whereas H's of the –CH_3 group of the thioamidate appear at 3.51 ppm. In the case of [Ag(atdzt)(PPh_3)] (**3**), signals of the H's of the phenyl groups of the PPh3 moieties appear in the 7.66-7.30 ppm region as a set of partially resolved multiplets.

S2.2.2 Stability study followed by UV-vis spectroscopy

pH= 7.4

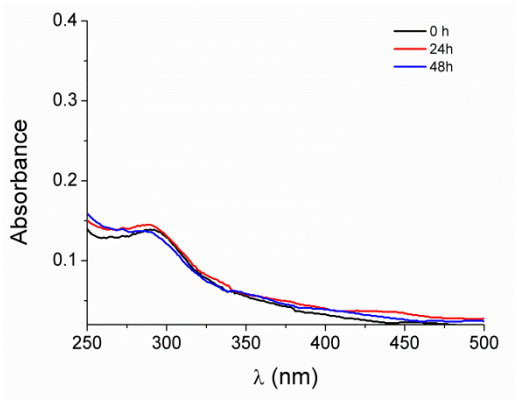

[Ag(atdztH)(xantphos)Cl] (1)

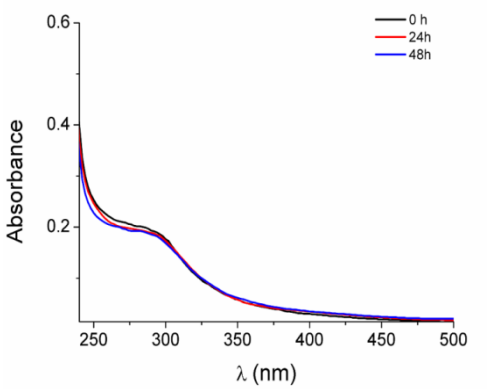

[Ag(atdztH)(DPEphos)]$_2$(NO$_3$)$_2$ (2)

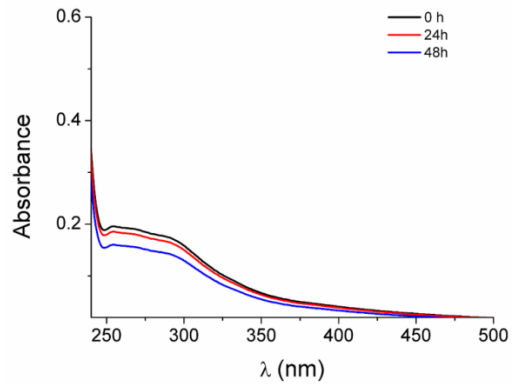

[Ag(atdzt)(PPh$_3$)$_3$] (3)

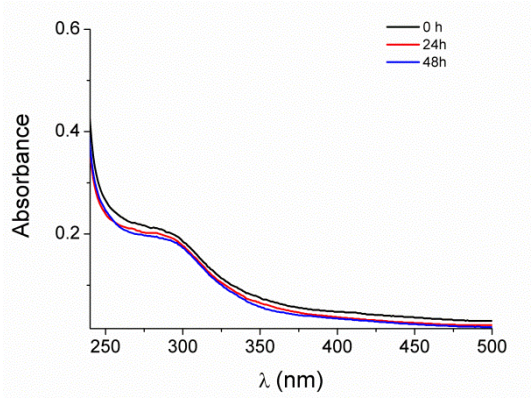

[Ag(atdzt)(DPEphos)]$_2$ (4)

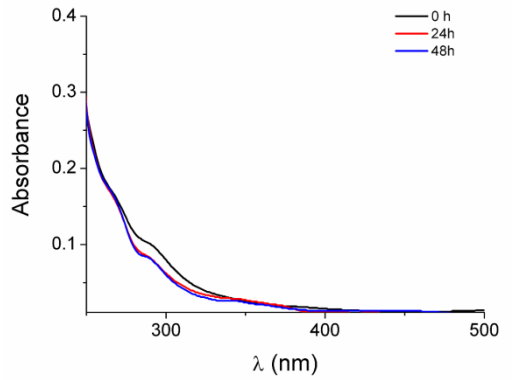

[Ag(mtft)(DPEphos)]$_2$ (5)

(continued)

pH= 6.0

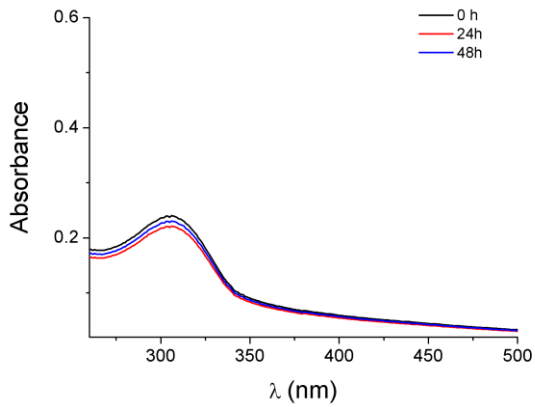

[Ag(atdztH)(xantphos)Cl] (1)

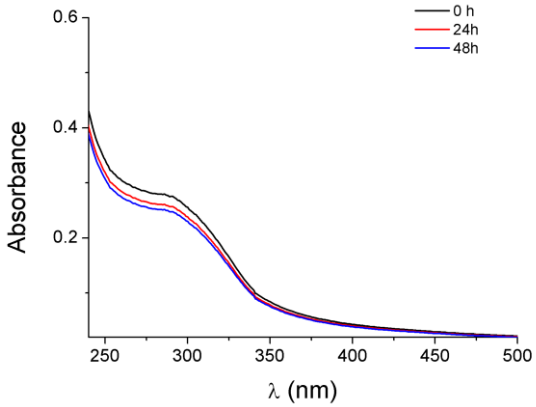

[Ag(atdztH)(DPEphos)]$_2$(NO$_3$)$_2$ (2)

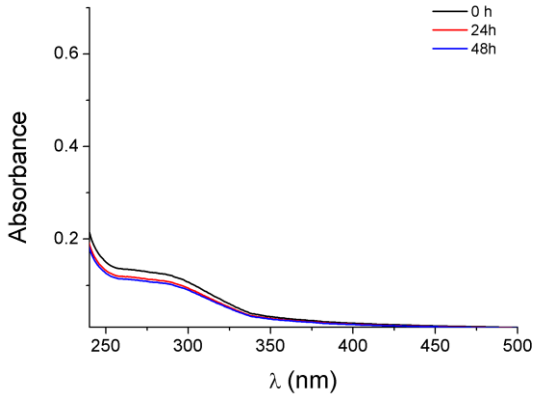

[Ag(atdzt)(PPh$_3$)$_3$] (3)

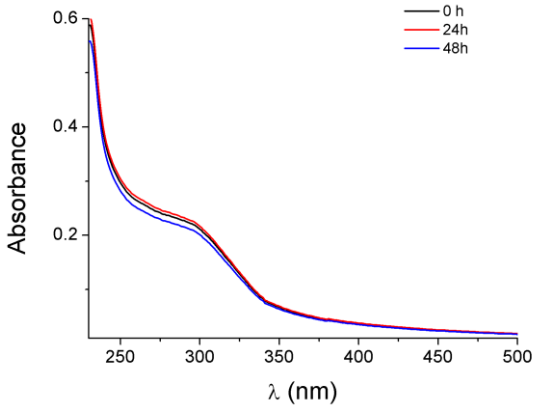

[Ag(atdzt)(DPEphos)]$_2$ (4)

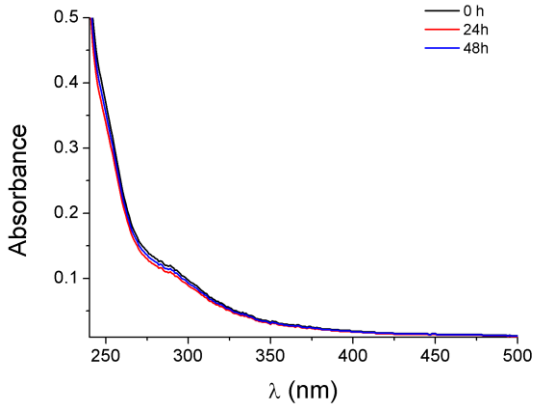

[Ag(mtft)(DPEphos)]$_2$ (5)

Figure S6. UV-vis absorption spectra of **1-5** in PBS saline buffer solutions (10^{-6} M) at pH = 7.4 and acidic phosphate buffer (10^{-6} M) at pH = 6.0, at 0, 24 and 48 h time intervals.

S2.3 *In vitro* antibacterial activity

Table S8 *In vitro* antibacterial activity of **1-5**, and their ligands atdztH, mtftH, xantphos, PPh_3, and DPEphos in free form, evaluated by the minimum inhibitory concentration (MIC) and the half-minimum inhibitory concentration (IC_{50}) values (in μg/mL, and in μM of values in parentheses) provided by a nonlinear curve fit-growth/sigmoidal-dose response on the experimental optical density data. Values are expressed as mean ± standard deviation (SD) of three replicate measurements (with the exception of values higher than 100 μg/mL).

Compound	*E. coli*		*S. aureus*		*B. subtilis*		*B. cereus*	
	MIC	IC_{50}	MIC	IC_{50}	MIC	IC_{50}	MIC	IC_{50}
	μg/mL (μM)		μg/mL (μM)		μg/mL (μM)		μg/mL (μM)	
1	60 (70)	7.6 (8.9±0.5)	73 (85.4)	19 (22.6±1.3)	100 (117)	53 (61.9±2.7)	100 (117)	30 (35.0±2.8)
2	>100 (64)	78.1 (46.6±4.6)	100 (64)	3.2 (2.0±0.2)	50 (31)	8 (5±0.4)	50 (32)	5.1 (3.3±0.15)
3	>100	>100	>100	18 (17.5±1.4)	>100	25 (24.3±2.0)	>100	32 (31.7±1.7)
4	100 (64)	6 (3.9±0.1)	100 (64)	4.3 (2.7±0.2)	100 (64)	37 (23.6±0.8)	100 (64)	17.1 (11.0±0.4)
5	>100 (> 61)	85.8 (52.7±4.5)	>100 (61)	100 (61)	>100 (> 61)	>100 (> 61)	>100 (61)	>100 (> 61)
atdztH	>100 (>750)	>100 (>750)	>100 (>750)	40 (300±15.5)	>100 (>750)	40 (300±15.0)	>100 (750)	60 (450±22.0)
mtftH	>100 (>500)	>100 (>500)	>100 (500)	100 (500)	>100 (>500)	>100 (>500)	>100 (500)	>100 (>500)
DPEphos	>100(186)	>100 (186)	>100 (186)	65 (116±6.8)	>100 (186)	48 (78±5.0)	>100(186)	47 (88±5.6)
xantphos	>100	50 (86±6.9)	>100	78 (135±6.5)	>100	65 (112±6.5)	>100	65 (112±6.9)
PPh_3	>100	51 (194±2.0)	>100	70 (267±2.2)	>100	>100 (>380)	>100	70 (267±9.0)
ampicillin	100	80 (229±8)	100	59 (169±7)	100	50 (143±4.2)	100	50 (142±5)

S2.4 *In vitro* anticancer activity

Table S9. Growth inhibition/cytostatic (GI_{50} and TGI, in μM) and cytocidal/cytotoxic (IC_{50}, in μM) effects induced by **1-5** against SKOV-3, Hup-T3, DMS114, and PC3 human cancer, and MRC5 human normal cell lines.

Complex	MRC5			SKOV-3			Hup-T3			DMS114			PC3		
	GI_{50} (μM)	TGI (μM)	IC_{50} (μM)	GI_{50} (μM)	TGI (μM)	IC_{50} (μM)	GI_{50} (μM)	TGI (μM)	IC_{50} (μM)	GI_{50} (μM)	TGI (μM)	IC_{50} (μM)	GI_{50} (μM)	TGI (μM)	IC_{50} (μM)
1	12.4±0.2	17.0±0.5	21.6±0.8	7.0±0. 5	9.3±0.8	11.7 ±0.8	2.6±0.2	4.5±0.2	9.2±0.2	3.0±0.02	5.0±0.1	9.2±0.25	5.0±0.05	8.1±0.15	11.3±0.2
2	3.5±0.5	6.5±0.5	10.0±0.8	2.0±0.2	3.2±0.3	4.5 ±0.3	1.8±0.5	3.4±0.4	8.0±0.4	2.0±0.08	3.0±0.1	4.0±0.25	1.2±0.03	2.9±0.2	4.1±0.5
3	1.4±0.05	2.5±0.18	4.0±0.2	1.0±0.05	2.3±0.1	4.0 ±0.2	1.9±0.05	3.1±0.2	4.5±0.2	1.0±0.04	2.6±0.24	4.2±0.25	1.1±0.05	2.8±0.25	4.2±0.2
4	80.0±3.5	>100	>100	25.0±1. 5	64.0±2.5	>100	77.5±0.8	97.5±1.5	>100	27.0±0.7	72.0±1.3	>100	20.0±0.5	92.0±0.8	>100
5	60.0±2.5	91.0±2.8	>100	28.0±1.0	43.0±1.3	84.0±1.8	33.0±0.2	48.0±0.2	>100	26.0±1.2	39.0±1.5	53.0±1.8	32.0±0.5	50.0±0.8	82.0±1.2

S2.5 *In vitro* antioxidant activity

Table S10. Scavenging ability (% scavenging) of **1-5**, atdztH, mtftH, PPh_3, xantphos, DPEPhos, and reference compounds NDGA, BHT, Trolox, L-ascorbic acid for H_2O_2 and DPPH and ABTS free radicals.

Compound	% Scavenging			
	H_2O_2	DPPH		ABTS
		30 min	60 min	
1	75.68±0.83	80.90±1.56	80.64±0.84	72.73±1.44
2	75.32±0.71	87.18±1.12	97.54±0.61	94.36±1.14
3	83.10±0.16	79.89±0.7	82.05±0.87	92.15±0.65
4	95.40±0.04	66.22±1.08	67.70±1.23	87.25±0.65
5	73.20±1.8	8.04±0.65	8.86±1.13	37.71±0.85
atdztH	94.15±0.35	52.02±1.08	57.10±0.87	63.17±1.34
mtftH	73.5±0.55	3.84±1.11	5.49±1.11	25.9±0.65
Xantphos	98.18±0.75	22.01±0.13	33.23±0.27	51.11±1.06
PPh_3	87.96±1.32	3±0.12	8.04±0.22	58.29±1.2
DPEphos	90.4±1.16	22.7±0.4	39.14±0.63	48.32±0.92
NDGA	Not tested	87.08±0.12	87.47±0.12	Not tested
BHT	Not tested	61.30±1.16	76.78±1.12	Not tested
Trolox	Not tested	Not tested		98.10±0.48
L-ascorbic acid	60.80±0.20	Not tested		Not tested

S2.6 CT-DNA interaction

S2.6.1 CT-DNA interaction followed by UV absorption spectroscopy

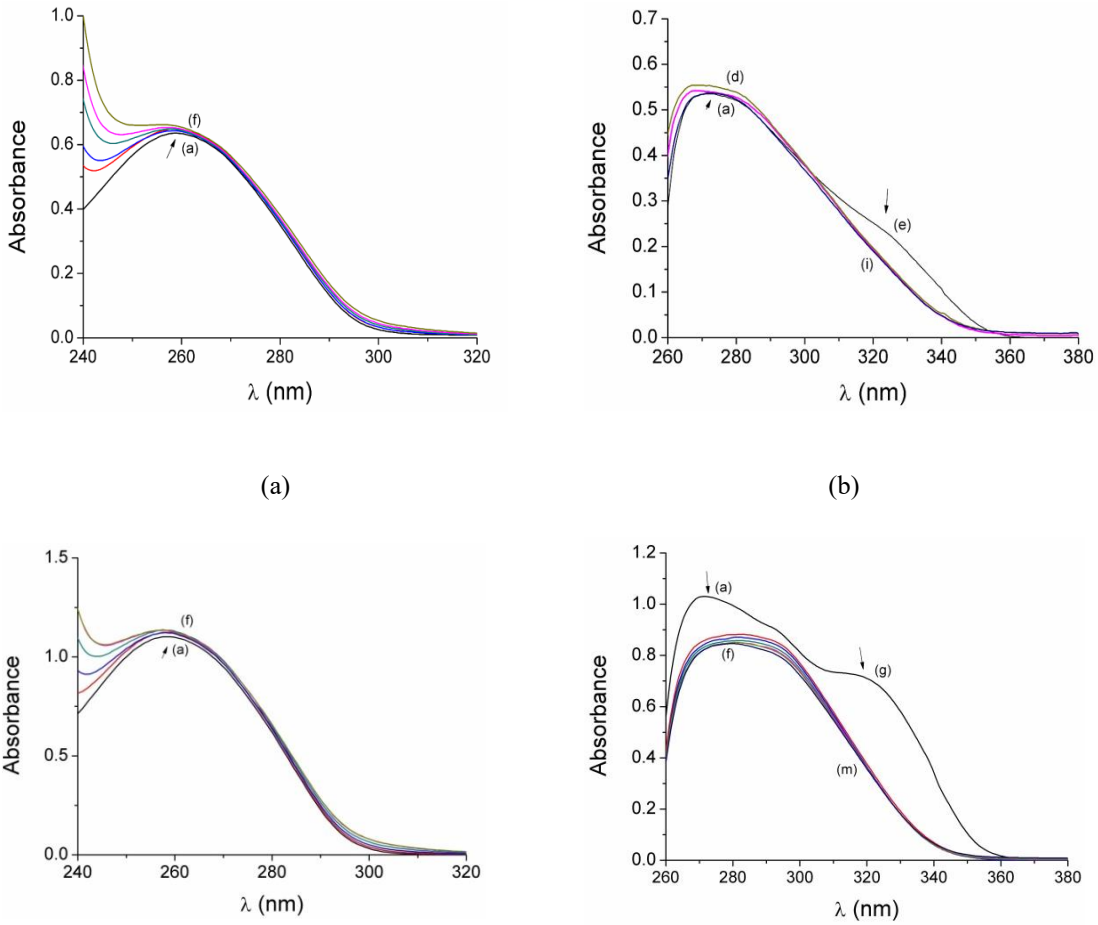

(a) (b)

(c) (d)

Figure S7 (a) and (c): UV-vis spectra of CT-DNA (0.15 mM) in buffer solution (150 mM NaCl and 15 mM trisodium citrate at pH 7.0) upon addition of increasing amounts of **1** and **2**, respectively (a→f). Arrows show the changes upon increasing concentrations of the compound. (b) and (d): UV-vis spectra of DMSO solutions of **1** and **2** (2.5×10^{-5} M) upon addition of increasing amounts of CT-DNA ([DNA]/[compound] = 0-0.8) (a→d, e→f for **1** and a→f, g→m for **2**). Arrows show the spectral changes upon increasing amounts of CT-DNA.

Table S11 Spectral changes of UV absorption bands of **1-3,** atdztH, xantphos, DPEphos and PPh_3 in solution in DMSO (2.5×10^{-5} M) upon addition of increasing concentrations of CT-DNA: wavelength of UV absorption band maximum (λ_{max}, nm), percentage of hyper/hypochromism ($\Delta A/A_o$, %), blue/red shift of λ_{max} ($\Delta\lambda$, nm) and CT DNA-binding constants (K_b, M^{-1}).

Compound	λ_{max}(nm) ($\Delta A/A_o$ (%)[a], $\Delta\lambda$ (nm)[b])	K_b (M^{-1})
1	272 (–3,+2), 322 (–46, elm[c])	$3.68(\pm0.14)\times10^4$
2	270 (–22,0), 294 (–12,0), 318 (–80,elm[c])	$7.38(\pm0.30)\times10^6$
3	267 (+4.5, +3), 320 (–60, elm[c])	$6.35(\pm0.05)\times10^7$
atdztH	320 (-22,-10)	$1.01(\pm0.24)\times10^6$
xantphos	272 (+43,0)	$1.66(\pm0.7)\times10^5$
DPEphos	270 (+49,0)	$1.94(\pm0.2)\times10^5$
PPh_3	268 (+24,+3)	$2.82(\pm0.2)\times10^6$

[a] "+" denotes hyperchromism, "–" denotes hypochromism
[b] "+" denotes red-shift, "–" denotes blue-shift
[c] ''elm" = eliminated

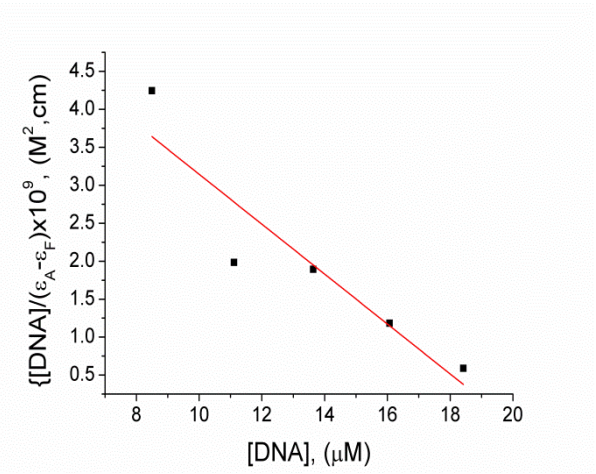

[AgCl(atdztH)(xantphos)] (1)

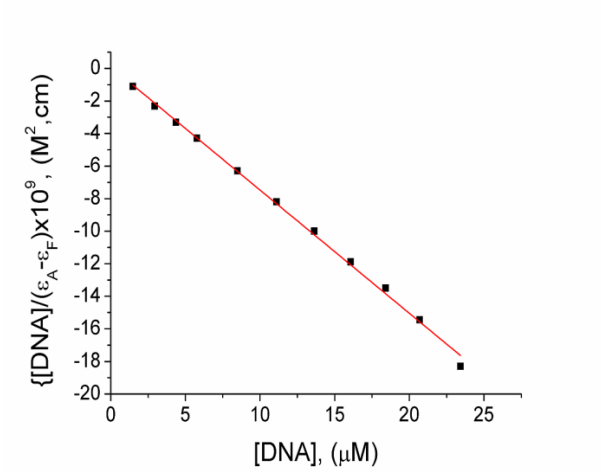

[Ag(μ-atdztH)(DPEphos)]$_2$(NO$_3$)$_2$ (2)

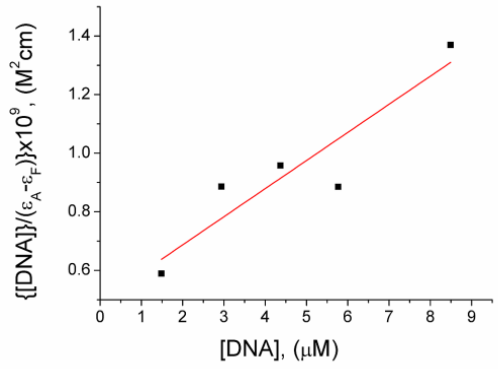

DPEphos

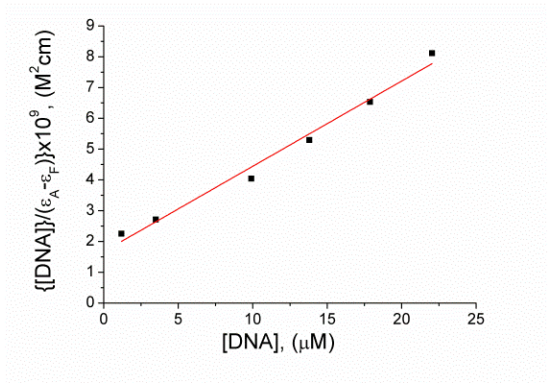

xantphos

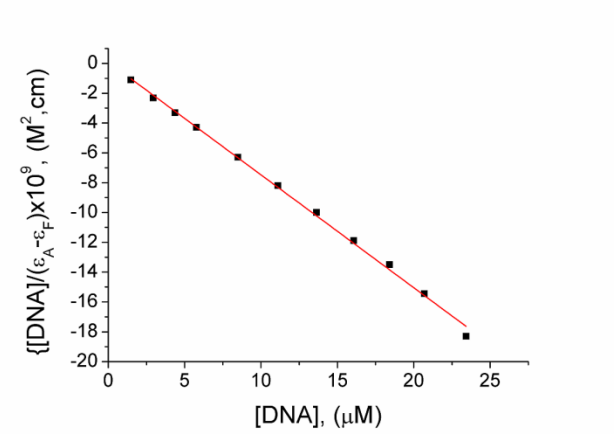

atdztH

Figure S8 Plots of [DNA]/(εA-εf) *versus* [DNA] for selected **1** and **2** and their corresponding ligands in their free form DPEphos, xantphos and atdztH

S2.6.2 CT-DNA interaction followed by viscosity measurements.

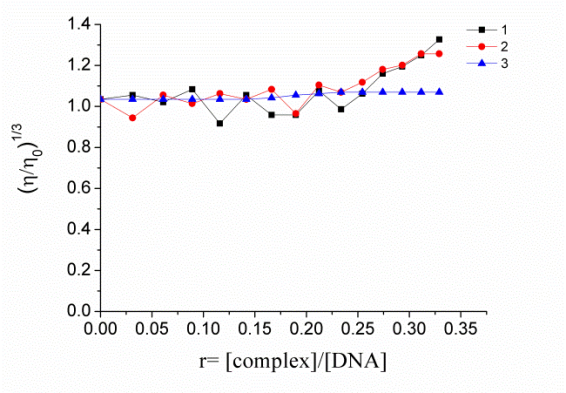

Figure S9. Relative viscosity $(\eta/\eta_o)^{1/3}$ changes of a CT-DNA (0.1 mM) buffered solution (150 mM NaCl and 15 mM trisodium citrate at pH 7.0) upon addition of increasing amounts of **1**, **2** and **3** *versus* r = [complex]/[DNA].

S2.6.2 EB competitive binding

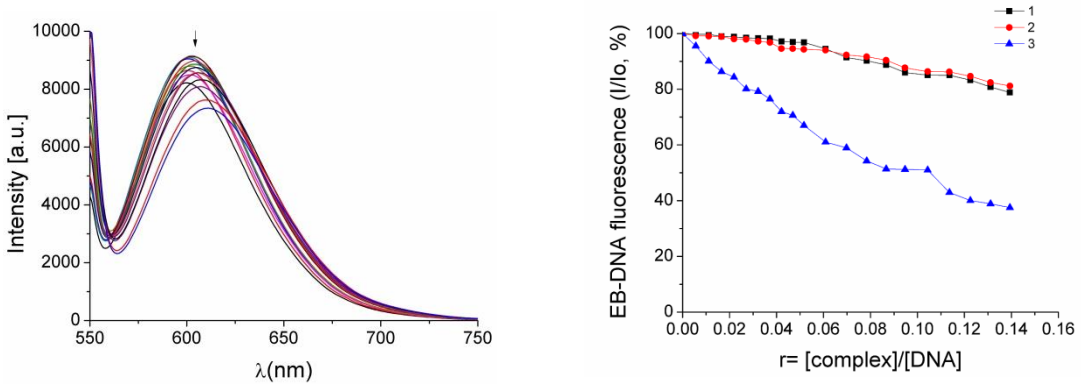

(a) (b)

Figure S10 (a) Fluorescence emission spectra (λ_{ex} = 540 nm) for EB–DNA ([EB] = 20 μM, [DNA] = 25 μM) in buffer solution in the absence and presence of increasing amounts of **2**. The arrow shows the changes of intensity upon increasing amounts of **2**. (b) Plot of EB-DNA relative fluorescence emission intensity (%I/I_0) at λ_{em} = 592 nm *vs.* *r* (*r* = [compound]/[DNA]) in buffer solution (150 mM NaCl and 15 mM trisodium citrate at pH 7.0) in the presence of **1**-**3** (quenching up to 23.2% of the initial EB–DNA fluorescence for **1**, 31.5% for **2** and 62.5% for **3**).

Table S12. Competitive binding studies of **1**, **2** and **3** with EB for CT-DNA: Percentage of EB-DNA fluorescence quenching at λ_{em}= 592 nm ($\Delta I/I_o$, %), Stern-Volmer constants (K_{SV}, M^{-1}) and fluorescence quenching constants (k_q, $M^{-1}s^{-1}$).

Complex	$\Delta I/I_0$ (%)	K_{SV} (M^{-1})	k_q ($M^{-1}s^{-1}$)
1	23.2	4.60 (±0.18)×10^4	2.00(±0.08)×10^{12}
2	31.5	3.77 (±0.14)×10^4	1.37(±0.06)×10^{12}
3	62.5	1.02(±0.04)×10^5	4.42(±0.16)×10^{12}

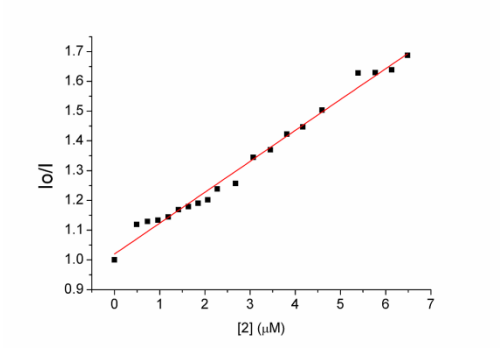

[Ag(dmp2SH)(PPh_3)$_2$](NO_3) (2)

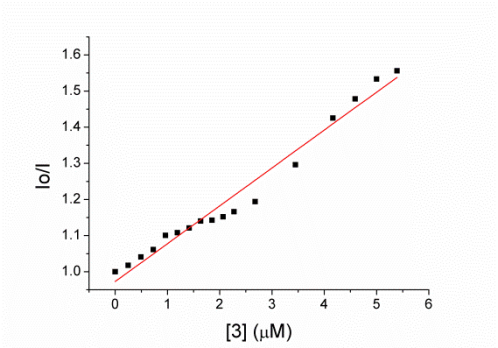

[Ag(dmp2SH)(xantphos)](NO_3) (3)

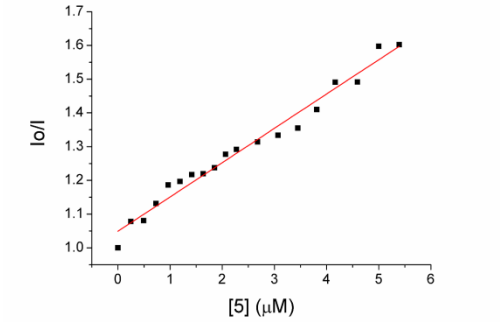

[Ag(dmp2S)(xantphos)] (5)

Figure S11 Stern-Volmer plots of quenching EB-DNA fluorescence for **1**-**3**.

S2.7 Serum albumins binding

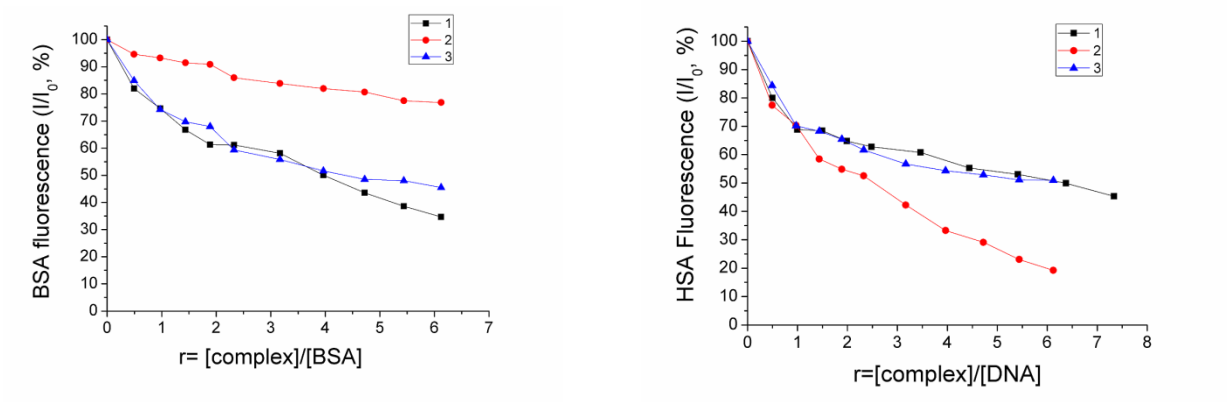

Figure S12. Plots of percentage of fluorescence intensity changes (I/I_o, %) at λ(em) = 350 nm of (a) BSA and (b) HSA in buffer solutions (150 mM NaCl and 15 mM trisodium citrate at pH = 7.0) upon addition of increasing amounts of complexes **1**, **2** and **3** *versus* r = [complex]/[BSA] and r = [complex]/[HSA], respectively

Table S13. Emission quenching constants (k_q) and binding constants (K) for the interaction of 1, 2 and 3 with BSA and HSA.

Complex	BSA		HSA	
	k_q ($M^{-1}s^{-1}$)	K (M^{-1})	k_q ($M^{-1}s^{-1}$)	K (M^{-1})
1	$9.36(\pm0.08)\times10^{12}$	$1.36(\pm0.08)\times10^{5}$	$4.49(\pm0.22)\times10^{12}$	$4.87(\pm0.22)\times10^{5}$
2	$1.61(\pm0.4)\times10^{12}$	$4.76(\pm0.4)\times10^{4}$	$1.88(\pm0.08)\times10^{13}$	$1.13(\pm0.08)\times10^{5}$
3	$7.23(\pm0.08)\times10^{12}$	$1.89\ (\pm0.08)\times10^{5}$	$6.73(\pm0.07)\times10^{12}$	$2.33(\pm0.07)\times10^{5}$

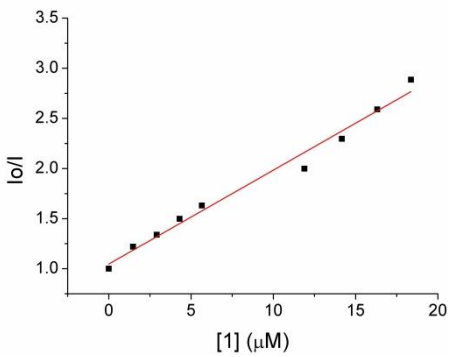

[Ag(atdztH)(xantphos)Cl] (1)

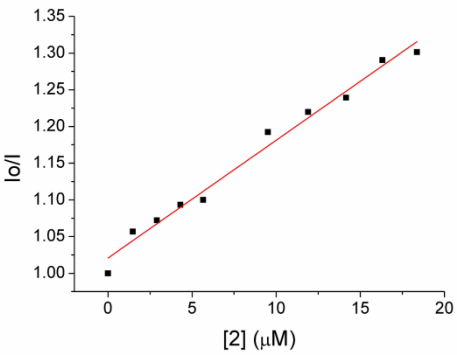

[Ag(atdztH)(DPEphos)]$_2$(NO$_3$)$_2$(2)

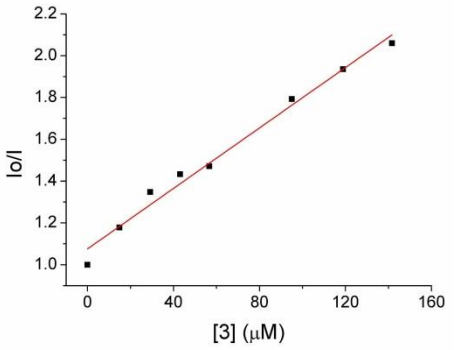

[Ag(atdzt)(PPh$_3$)$_3$] (3)

Figure S13. Stern Volmer quenching plots of BSA for **1**-**3**.

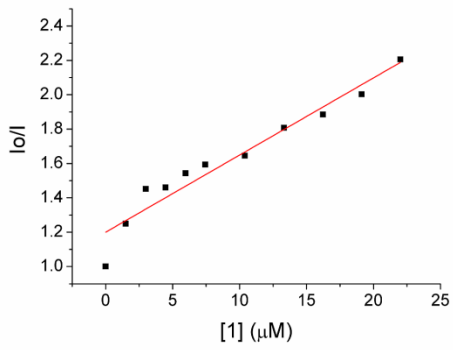

[Ag(atdztH)(xantphos)Cl] (1)

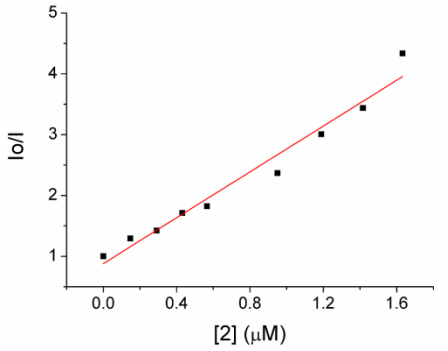

[Ag(atdztH)(DPEphos)]$_2$(NO$_3$)$_2$ (2)

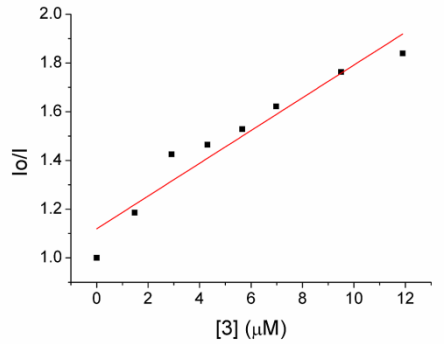

[Ag(atdztH)(PPh$_3$)$_3$] (3)

Figure S14. Stern Volmer quenching plots of HSA for **1**-**3**.

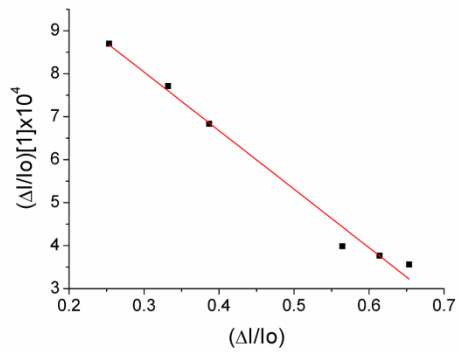

[Ag(atdztH)(xantphos)Cl] (1)

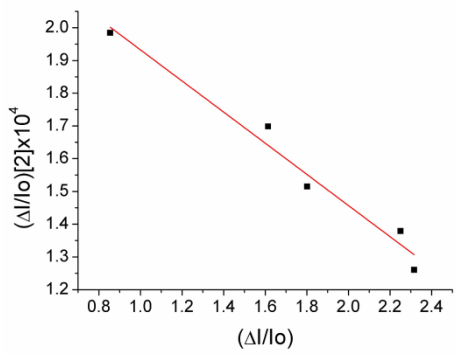

[Ag(atdztH)(DPEphos)]$_2$(NO$_3$)$_2$ (2)

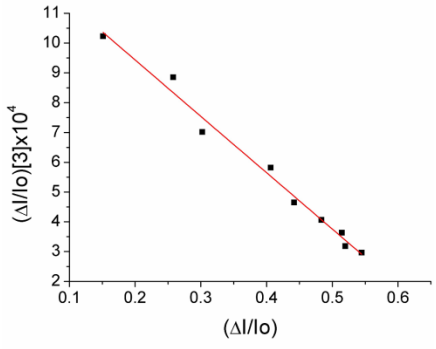

[Ag(atdzt)(PPh$_3$)$_3$] (3)

Figure S15. Scatchard quenching plots of BSA for **1**-**3**.

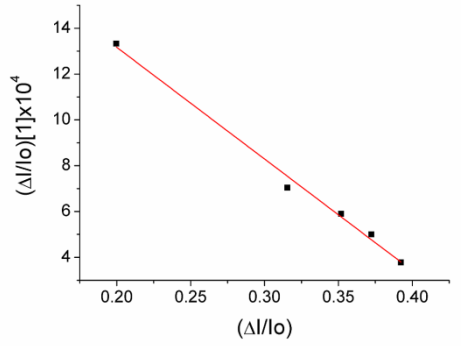

[Ag(atdztH)(xantphos)Cl] (1)

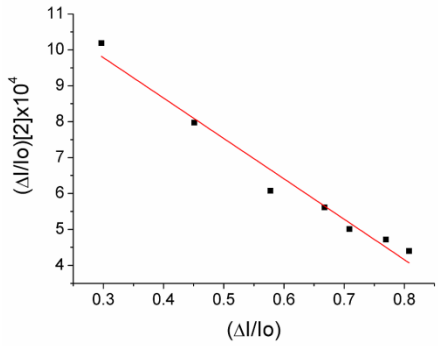

[Ag(atdztH)(DPEphos)]$_2$(NO$_3$)$_2$ (2)

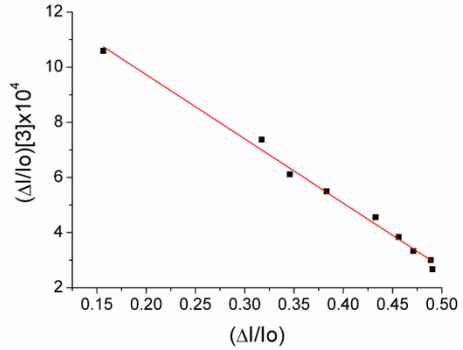

[Ag(atdzt)(PPh$_3$)$_3$] (3)

Figure S16. Scatchard quenching plots of HSA for **1**-**3**.

S2.8 Molecular docking calculations

Table S14. Binding interactions of lowest energy binding pose of **1** and **4** with *E. coli* DNA gyrase, and **2** and **3** with *S. aureus* DNA gyrase (PDB accession numbers: 1KZN, and 5CDM, respectively). Common contacts with CBN are denoted with asterisk (Atom numbering and bond lengths are derived from PyMol software) (type of interaction: H-b: hydrogen bond, H-ph: hydrophobic, π-alkyl: pi-alkyl hydrophobic, π-anion and π-cation: pi-charged electrostatic interactions, π-polar: pi-polar), P: polar.

Complex 1 ligand	***E. coli* DNA gyrase amino acid residue**	**Bond length (Å)**	**Type**
atdztH	*Pro (P79)/Cβ	2.9	P
	*Ala (A86)/Cβ	3.9	P
	*Ile (I90)/Cγ1	3.7	P
xantphos	*Asn (N46)/Nδ2	2.4	π-polar
	*Asn (N46)/O	2.9	π-polar
	*Glu (E50)/Cγ	3.0	π-alkyl
	*Glu (E50)/Oε1	3.7	π-anion
	*Glu (E50)/Oε2	2.4	π-anion
	*Asp (D49)/Cβ	3.6	π-alkyl
	*Asp (D49)/Oδ1	3.0	π-polar
	*Asp (D49)/O	3.7	P
	*Arg (R76)/Nε	3.0	π-cation
	*Arg (R76)/Nη1	2.8	π-cation
	*Arg (R76)/Cβ	3.2	π-alkyl
	*Arg (R136)/Nη1	3.8	π-cation
	*Pro (P79)/Cδ	2.8	π-alkyl
	*Gly (G77)/O	2.6	π-polar
	*Ile (I78)/Cα	2.9	π-alkyl
	Ala (A53)/Cβ	2.7	H-ph
Complex 4 ligand	***E. coli* DNA gyrase amino acid residue**	**Bond length (Å)**	**Type**
atdzt	*Pro (P79)/N	3.7	H-b
	*Pro (P79)/Cδ	3.7	P
	*Ile (I78)//Cγ2	2.8	P
DPEphos	*Asp (D49)/O	2.5	π-polar
	*Asp (D49)/Oδ1	2.8	π-anion
	*Glu (E50)/Oε1	2.6	π-anion
	*Arg (R76)/Nη2	2.7	π-cation
	*Asn (N46)/Nδ2	3.8	π-polar
	*Asn (N46)/O	3.2	π-polar
	His (H95)/O	2.9	π-alkyl
	Ala (A96)/O	2.4	π-polar
Complex 2 ligand	**S. aureus DNA gyrase amino acid residue/ DNA Pyrimidine-Purine**	**Bond length (Å)**	**Type**
atdztH	Arg (R272)/Nε (chain A)	2.2	H-b
	Arg (R272)/Nη2 (chain A)	3.3	H-b
	dG'3/OP1 (chain E)	2.2	P
	dG'3/OP2 (chain E)	2.9	P

	dC'2012/N4H41 (chain N)	2.2	H-b
	dC'2012/C5 (chain N)	2.9	P
	dC'2011/C5 (chain N)	3.5	P
DPEphos	Gly (G115)/O (chain A)	2.3	π-polar
	Gly (G115)/C (chain A)	3.8	π-alkyl
	Gly (G117)/Cα (chain A)	2.8	π-alkyl
	Asp (D116)/N (chain A)	3.8	π-polar
	Asp (D116)/Cα (chain A)	3.6	π-alkyl
	Asn (N269)/Nδ2 (chain A)	2.6	π-polar
	dC'2011/OP1 (chain N)	2.5	π-polar
	dC'2012/OP2 (chain N)	2.3	π-polar
	dG'2013/OP2 (chain N)	2.5	π-polar
	dG'2013/N7 (chain N)	2.5	π-polar
	dG'3/N7 (chain E)	3.8	π-polar
	dG'3/C2' (chain E)	3.9	π-alkyl
Complex 3 ligand	**S. aureus DNA gyrase amino acid residue/ DNA Pyrimidine-Purine**	**Bond length (Å)**	**Type**
atdzt	Asp (D83)/Oδ1 (chain C)	3.7	H-b
	Glu (E88)/Oε1 (chain C)	3.6	H-b
	Tyr (Y87)/Cβ (chain C)	3.9	P
	Met (M121)/Cε (chain C)	2.9	P
	Ser (S84)/Cα (chain C)	2.3	P
	Ser (S84)/OγH (chain C)	2.1	H-b
PPh_3	Asp (D83)/Oδ2 (chain C)	2.3	π-anion
	Arg (R122)/Nη2 (chain A)	3.8	π-cation
	Arg (R122)/N (chain A)	3.0	π-polar
	Arg (R122)/Cδ (chain A)	2.9	π-alkyl
	Ala (A120)/Cβ (chain A)	2.6	π-alkyl
	Met (M121)/Cε (chain A)	2.6	π-alkyl
	Met (M121)/Cγ (chain A)	3.4	π-alkyl
	Arg (R122)/Cδ (chain C)	3.3	π-alkyl
	Arg (R122)/Cβ (chain C)	3.4	π-alkyl
	Ala (A120)/Cβ (chain C)	3.4	π-alkyl
	dC'2011/N4 (chain I)	2.2	π-polar
	dG'2009/N7 (chain I)	2.6	π-polar
	dG'2009/O6 (chain I)	2.6	π-polar
	dG'2009/C2' (chain I)	2.7	π-alkyl
	dG'2010/N7 (chain I)	3.7	π-polar
	dG'2010/O6 (chain I)	2.3	π-polar
	dG'2009/C8 (chain I)	3.9	π-alkyl
	dC'2012/N4 (chain I)	3.2	π-polar
	dG'2009/N7 (chain N)	3.0	π-polar
	dG'2010/O6 (chain N)	2.9	π-polar
	dG'2010/N7 (chain N)	3.3	π-polar
	dC'2011/N4 (chain N)	2.3	π-polar
	dG'2009/O6 (chain N)	3.0	π-polar

	dG'2009/N7 (chain N)	2.3	π-polar
	dG'2010/N1 (chain N)	3.9	π-polar
	dG'2009/C2' (chain N)	3.1	π-alkyl

Table S15. Binding interactions of lowest energy binding pose of **3** with Fibroblast Growth Factor Receptor 1 (FGFR1) (PDB accession number: 4V04) (Atom numbering and bond lengths are derived from PyMol software) (type of interaction: π-π: pi-pi displaced and T-shaped, π-alkyl: pi-alkyl hydrophobic, π-anion and π-cation: pi-charged electrostatic interactions, π-polar: pi-polar). Asterisk denotes common binding contacts with ponatinib.

Complex 3 ligand	**Amino acid residue**	**Bond length (Å)**	**Type**
PPh_3	*Phe (F642)	2.4-3.3	π-π displaced, π-π T-shaped
	Arg (R570)/Nη2	2.7	π-cation
	Asn (N659)/Oδ1	3.7	π-polar
	Thr (T658)/Cγ2	2.9	π-alkyl
	Asn (N568)/N	2.9	π-polar
	Asn (N568)/Nδ2	2.6	π-polar
	Arg (R627)/Cδ	2.2	π-alkyl
	Arg (R627)/O	3.1	π-polar
	Glu (E571)/Oε1	2.1	π-anion
	Glu (E486)/O	2.9	π-polar
	Glu (E486)/N	2.1	π-polar
	Glu (E486)/Ca	2.0	π-alkyl
	Gly (G485)/O	2.1	π-polar
	Gly (G490)/O	3.2	π-polar
	*Val (V492)/Cγ2	2.8	π-alkyl
	*Leu (L484)/O	3.0	π-polar
atdzt	Thr (T658)/Oγ1	2.6	π-polar
	Glu (E486)/O	3.6	π-polar

REFERENCES

1 Bruker Analytical X-ray Systems, Inc., 2006. Apex2, Version 2 User Manual, M86-E01078, Madison, WI.

2 P. W. Betteridge, J. R. Carruthers, R. I. Cooper, K.Prout, D. J. J. Watkin, CRYSTALS version 12: software for guided crystal structure analysis, Appl. Cryst., 2003, 36, 1487–1487.

3 C. F. Macrae, P. R. Edgington, P. McCabe, E. Pidcock, G. P. Shields, R. Taylor, M. Towler, J. van de Streek, Mercury: visualization and analysis of crystal structures.,J. Appl. Cryst., 2006, 39, 453–457.

4 J. M. Andrews, Determination of minimum inhibitory concentrations, J. Antimicrob. Chemother., 2001, 48 (Suppl. S1), 5–16

5 M. A. Tsiaggali, E.G. Andreadou, A.G. Hatzidimitriou, A.A. Pantazaki, P. Aslanidis, Copper (I) halide complexes of N-methylbenzothiazole-2-thione: Synthesis, structure, luminescence, antibacterial activity and interaction with DNA, J. Inorg. Biochem., 2013, 121, 121–128.

6 G. J. Finlay, W. R. Wilson, B. C. Baguley, Comparison of the in vitro activity of the cytotoxic drugs towards human carcinoma and leukemia cell lines, Eur. J. Cancer Clin. Oncol., 1986, 22, 655–662.

7 M. C. Alley, D. A. Scudiero, A. Monks, M. L. Hursey, M. J. Czerwinski, D. L. Fine, B. J. Abbott, J. G. Mayo, R. H. Shoemaker, M. R. Boyd, Feasibility of drug screening with panels of human tumor cell lines using a microculture tetrazolium assay, Cancer Res., 1988, 48, 589–601.

8 D.T. Trafalis, C. Camoutsis, P. Karamanakos, A. Arvanitis, E. Tegou, N. Ziras, A.E. Athanassiou, Preclinical evaluation of the homo-aza-steroid ester 13-hydroxy-13-amino-13,17- seco-5-androstan-17-oic-13,17-lactam-p-bis(2-chloroethyl)aminophenoxy acetate for the treatment of malignant melanoma, J. BUON., 2003, 8, 333–339.

9 R. J. Ruch, C. Cheng, J. E. Klaunig, Prevention of cytotoxicity and inhibition of intercellular communication by antioxidant catechins isolated from Chinese green tea, Carcinogenesis, 1989, 10, 1003-1008.

10 D. Li, J. Tian, W. Gu, X. Liu, S. Yan, A novel 1,2,4-triazole-based copper(II) complex: Synthesis, characterization, magnetic property and nuclease activity, J. Inorg. Biochem., 2010, 104, 171–179.

11 J.R. Lakowicz, Principles of Fluorescence Spectroscopy, 3rd ed, Plenum Press, New York, 2006.

12 G. Zhao, H. Lin, S. Zhu, H. Sun, Y. Chen, Dinuclear palladium(II) complexes containing two monofunctional $[Pd(en)(pyridine)Cl]^+$ units bridged by Se or S. Synthesis, characterization, cytotoxicity and kinetic studies of DNA-binding, J. Inorg. Biochem., 1998, 70, 219–226.

13 D. P. Heller, C. L. Greenstock, Fluorescence lifetime analysis of DNA intercalated ethidium bromide and quenching by free dye, Biophys. Chem., 1994, 50, 305–312.

14 Spartan ’14 v.1.1.4, Wavefunction Inc., Irvine, CA, USA; www.wavefun.com.

15 D. Lafitte, V. Lamour, P.O. Tsvetkov, A.A. Makarov, M. Klich, P. Deprez, D. Moras, C. Briand, R. Gilli, DNA gyrase interaction with coumarin-based inhibitors: the role of the hydroxybenzoate isopentenyl moiety and the 5'-methyl group of the noviose, Biochemistry, 2002, 41, 7217–7223.

16 P. F. Chan, V. Srikannathasan, J. Huang, H. Cui, A. P. Fosberry, M. Gu, M. M. Hann, M. Hibbs, P. Homes, K. Ingraham, J. Pizzollo, C. Shen, A. J. Shillings, C. E. Spitzfaden, R. Tanner, A. J. Theobald, R. A. Stavenger, B. D. Bax, M. N. Gwynn, Structural basis of DNA gyrase inhibition by antibacterial QPT-1, anticancer drug etoposide and moxifloxacin. Nat. Commun., 2015, 6, 10048–10061.

17 J. A. Tucker, T. Klein, J. Breed, A. L. Breeze, R. Overman, C. Phillips, R. A. Norman, Structural Insights into FGFR Kinase Isoform Selectivity: Diverse Binding Modes of AZD4547 and Ponatinib in Complex with FGFR1 and FGFR4, Structure, 2014, 22, 1764–1774.

18 H. M. Berman, J. Westbrook, Z. Feng, G. Gilliland, T. N. Bhat, H. Weissig, I. N. Shindyalov, P. E. Bourne, The Protein Data Bank, Nucleic Acids Res., 2000, 28, 235-242.

19 H. M. Berman, K. Henrick, H. Nakamura, Announcing the worldwide Protein Data Bank, Nature Struct. Mol. Biol., 2003, 10, 980.

20 F.C. Bernstein, T.F. Koetzle, G.J. Williams, E.E. Meyer, M.D. Brice, J.R. Rodgers, O. Kennard, T. Shimanouchi, M. Tasumi, The Protein Data Bank: a computer-based archival file for macromolecular structures, J. Mol. Biol., 1977, 112, 535–542.

21 K. Fosgerau, T. Hoffmann, Peptide therapeutics: current status and future directions, Drug Discov. Today 2015, 20, 122–128.

22 D. Shivakumar, J. Williams, Y. Wu, W. Damm, J. Shelley, W. Sherman, Prediction of Absolute Solvation Free Energies using Molecular Dynamics Free Energy Perturbation and the OPLS Force Field, J. Chem. Theory Comput., 2010, 6, 1509–1519.

23 Schrödinger, http://www.schrodinger.com

24 G. M. Sastry, M. Adzhigirey, T. Day, R. Annabhimoju, W. Sherman, Protein and ligand preparation: parameters, protocols, and influence on virtual screening enrichments., J. Comput. Aided Mol. Des., 2013, 27, 221–234.

25 R. A. Friesner, R. B. Murphy, M. P. Repasky, L. L Frye, J. R. Greenwood, T. A. Halgren, P. C. Sanschagrin, D. T. Mainz, Extra precision glide: docking and scoring incorporating a model of hydrophobic enclosure for protein-ligand complexes J. Med. Chem., 2006, 49, 6177–6196.

26 T. A. Halgren, R. B. Murphy, R. A. Friesner, H. S. Beard, L. L. Frye, W. T. Pollard, J. L. Banks, Glide: a new approach for rapid, accurate docking and scoring. 2. Enrichment factors in database screening, J. Med. Chem., 2004, 47, 1750–1759.

27 M. P. Jacobson, D. L. Pincus, C. S. Rapp, T. J. F. Day, B. Honig, D. E. Shaw, R. A. Friesner, Proteins: Structure, Function and Bioinformatics, 2004, 55, 351–367.

28 T. A. Halgren, New method for fast and accurate binding-site identification and analysis, Chem Biol Drug Des., 2007, 69, 146-148.

29 T. A. Halgren, Identifying and Characterizing Binding Sites and Assessing Druggability, J. Chem. Inf. Model., 2009, 49, 2, 377–389.

30 R. A. Friesner, J. L. Banks, R. B. Murphy, T. A. Halgren, J. J. Klicic, D. T. Mainz, M. P. Repasky, E. H. Knoll, D. E. Shaw, M. Shelley, J. K. Perry, P. Francis, P. S. Shenkin, Glide: a new approach for rapid, accurate docking and scoring. 1. Method and assessment of docking accuracy, J. Med. Chem., 2004, 47, 1739–1749.

31 R. Farid, T. Day, R. A. Friesner, R. A. Pearlstein, New insights about HERG blockade obtained from protein modeling, potential energy mapping, and docking studies, Bioorg. Med. Chem., 2006, 14, 3160–3173.

32 G. D. Geromichalos, C. E. Alifieris, E. G. Geromichalou, D. T. Trafalis, Overview on the current status of virtual high-throughput screening and combinatorial chemistry approaches in multi-target anticancer drug discovery; Part I, J. BUON, 2016, 21, 764–779.

33 W. L. DeLano, The PyMOL Molecular Graphics System 0.99, DeLano Scientific, San Carlos, CA, USA, 2006.